






# Magnon orbital angular momentum of ferromagnetic honeycomb and zigzag lattice models

Randy S. Fishman <sup>1,\*</sup>, Tom Berlijn <sup>1</sup>, Jack Villanova <sup>2</sup>, and Lucas Lindsay <sup>1</sup>

<sup>1</sup>Materials Science and Technology Division, Oak Ridge National Laboratory, Oak Ridge, Tennessee 37831, USA

<sup>2</sup>Center for Nanophase Materials Sciences, Oak Ridge National Laboratory, Oak Ridge, Tennessee 37831, USA

 (Received 30 August 2023; revised 9 November 2023; accepted 9 November 2023; published 4 December 2023)

By expanding the gauge  $\lambda_n(\mathbf{k})$  for magnon band  $n$  in harmonics of momentum  $\mathbf{k} = (k, \phi)$ , we demonstrate that the only observable component of the magnon orbital angular momentum  $O_n(\mathbf{k})$  is its angular average over all angles  $\phi$ , denoted by  $F_n(k)$ . Although  $F_n(k)$  vanishes for antiferromagnetic honeycomb and zigzag ( $0 < J_1 < J_2$ ) lattices, it is nonzero for the ferromagnetic (FM) versions of those lattices in the presence of Dzyaloshinskii-Moriya interactions. For a FM zigzag model with equal exchange interactions  $J_{1x}$  and  $J_{1y}$  along the  $x$  and  $y$  axes, the magnon bands are degenerate along the boundaries of the Brillouin zone with  $k_x - k_y = \pm\pi/a$  and the Chern numbers  $C_n$  are not well defined. However, a revised model with  $J_{1y} \neq J_{1x}$  lifts those degeneracies and produces well-defined Chern numbers of  $C_n = \pm 1$  for the two magnon bands. When  $J_{1y} = J_{1x}$ , the thermal conductivity  $\kappa^{xy}(T)$  of the FM zigzag lattice is largest for  $J_2/J_1 > 6$  but is still about four times smaller than that of the FM honeycomb lattice at high temperatures. Due to the removal of band degeneracies,  $\kappa^{xy}(T)$  is slightly enhanced when  $J_{1y} \neq J_{1x}$ .

DOI: [10.1103/PhysRevB.108.214402](https://doi.org/10.1103/PhysRevB.108.214402)

## I. INTRODUCTION

The past 13 years have seen remarkable advances in the field of “magnonics” [1–3], which focuses on the quanta of spin excitations known as magnons. One of the main goals of magnonics is the storage and processing of information. Because they can travel over centimeter distances without incurring any costs in Joule heating [4], magnons offer many advantages over electrons in the next generation of technological devices. Due to their much lower velocities, magnons are also better suited than electrons to creating small devices. In quick succession, experimentalists have discovered that magnons can produce the thermal Hall [5–10] and Seebeck [11,12] effects.

Almost all previous theoretical work in magnonics has been based on the Berry curvature, which produces a fictitious magnetic field in the presence of dipole [13] or Dzyaloshinskii-Moriya (DM) [14] interactions. DM interactions are created by spin-orbit (SO) coupling. Because it was borrowed from the theory of electronic structure [15–17], the Berry phase is usually formulated in a semiclassical language. For a Bloch function  $|u_n(\mathbf{k})\rangle$  with energy  $\epsilon_n(\mathbf{k}) = \hbar\omega_n(\mathbf{k})$ , the Berry curvature

$$\mathbf{\Omega}_n(\mathbf{k}) = \frac{i}{2\pi} \left\{ \frac{\partial}{\partial \mathbf{k}} \times \langle u_n(\mathbf{k}) | \frac{\partial}{\partial \mathbf{k}} | u_n(\mathbf{k}) \rangle \right\} \quad (1)$$

of a ferromagnetic (FM) insulator requires that a magnon wave packet centered at  $\mathbf{r}_c$  obeys the equation of motion [15–17]

$$\frac{d\mathbf{r}_c}{dt} = \frac{\partial \epsilon_n(\mathbf{k})}{\hbar \partial \mathbf{k}} - \frac{d\mathbf{k}}{dt} \times \mathbf{\Omega}_n(\mathbf{k}). \quad (2)$$

Therefore, the Berry curvature causes the wave packet to bend away from the expected direction  $\partial \epsilon_n(\mathbf{k})/\partial \mathbf{k}$  for a free magnon with  $\mathbf{\Omega}_n(\mathbf{k}) = 0$ .

Prior to the first observation of the magnon Hall effect in the FM insulator  $\text{Lu}_2\text{V}_2\text{O}_7$  [5], it was predicted by Katsura *et al.* [18] based on a Kubo formula for the temperature dependence of the thermal conductivity  $\kappa^{xy}(T)$ . This Kubo formula involves an integral of the Berry curvature  $\mathbf{\Omega}_{nz}(\mathbf{k})$  perpendicular to the sample over the first Brillouin zone (BZ):

$$\kappa^{xy}(T) = -\frac{k_B^2 T}{2\pi \hbar} \sum_n \int_{\text{BZ}} d^2k c_2(\rho(\epsilon_n(\mathbf{k}))) \mathbf{\Omega}_{nz}(\mathbf{k}), \quad (3)$$

where  $\rho(\epsilon) = 1/[\exp(\epsilon/k_B T) - 1]$  is the Boltzmann distribution with zero chemical potential for magnons, and  $c_2(\rho)$  is defined in Sec. V. The above expression includes the effects of the magnon edge currents traveling around the sample as well as the effects of the magnon wave-packet “self-rotation” due to its orbital motion [19,20]. The prediction and subsequent observation of the magnon Hall effect based on the Berry curvature was one of the great early achievements in the field of magnonics.

Because of SO coupling, magnons carry both spin and orbital angular momentum. By constructing a Lagrangian that produces the correct equation of motion for the magnetization  $\mathbf{M}_i = 2\mu_B \mathbf{S}_i$  at site  $i$ , Tsukernik *et al.* [21,22] demonstrated that the orbital angular momentum (OAM) of magnons along  $\mathbf{z}$  can be written in terms of Bloch functions as

$$O_n(\mathbf{k}) = -\frac{i\hbar}{2} \left\{ \mathbf{k} \times \langle u_n(\mathbf{k}) | \frac{\partial}{\partial \mathbf{k}} | u_n(\mathbf{k}) \rangle \right\} \cdot \mathbf{z}. \quad (4)$$

But Tsukernik and co-workers failed to realize that the OAM defined above is not directly observable because, unlike the Berry curvature  $\mathbf{\Omega}_n(\mathbf{k})$ ,  $O_n(\mathbf{k})$  is not gauge-invariant [23].

\*Corresponding author: fishmanrs@ornl.gov

This can be seen by expanding the spin Hamiltonian  $H$  to second order in powers of the deviation of the spin operators  $\mathbf{S}_i$  from their equilibrium values. Then the Bloch functions  $|u_n(\mathbf{k})\rangle$  satisfy the eigenvalue equation

$$H_2|u_n(\mathbf{k})\rangle = \epsilon_n(\mathbf{k})|u_n(\mathbf{k})\rangle. \quad (5)$$

Because  $H_2$  is translationally invariant, a new Bloch function obtained by the transformation

$$|u_n(\mathbf{k})\rangle \rightarrow |u_n(\mathbf{k})\rangle e^{-i\lambda_n(\mathbf{k})} \quad (6)$$

also satisfies the above eigenvalue equation. Under this gauge transformation, the Berry curvature  $\Omega_n(\mathbf{k})$  of Eq. (1) remains unchanged, but the OAM of Eq. (4) changes to

$$\begin{aligned} O_n(\mathbf{k}) &\rightarrow O_n(\mathbf{k}) + \frac{\hbar}{2} \left( k_x \frac{\partial}{\partial k_y} - k_y \frac{\partial}{\partial k_x} \right) \lambda_n(\mathbf{k}) \\ &= O_n(\mathbf{k}) + \frac{\hbar}{2} \frac{\partial}{\partial \phi} \lambda_n(k, \phi), \end{aligned} \quad (7)$$

where the gauge  $\lambda_n(\mathbf{k}) = \lambda_n(k, \phi)$  depends only on the band index  $n$  and the two-dimensional wave vector  $\mathbf{k} = (k, \phi)$ . Quantities like  $O_n(\mathbf{k})$  that depend on a gauge  $\lambda_n(\mathbf{k})$  cannot be physically observed [23]. However, the average of  $O_n(\mathbf{k})$  over all angles  $\phi$ ,

$$F_n(k) = \int_0^{2\pi} \frac{d\phi}{2\pi} O_n(\mathbf{k}), \quad (8)$$

does not depend on the gauge  $\lambda_n(\mathbf{k})$  [24]. Therefore,  $F_n(k)$  can be physically observed.

Regarding the magnon Hall effect as an indirect observation of the magnon OAM, direct observation of the magnon OAM through the angular average  $F_n(k)$  should then be possible by coupling magnons to other particles and quasiparticles that carry OAM. For example, magnons may couple to chiral phonons [25] in crystals with broken inversion symmetry. High-energy electron beams separated into orbital components by a grating [26] may also couple directly to the magnon OAM.

In this paper, we demonstrate that  $F_n(k)$  is the *only* observable component of the OAM. We then evaluate  $F_n(k)$  for FM honeycomb (HC) and square zigzag (ZZ) lattices with DM interaction  $D$ . Along with their antiferromagnetic (AF) counterparts, these lattices are sketched in Fig. 1. Each model is described by the general Hamiltonian

$$\begin{aligned} H &= -\frac{1}{2} \sum_{i,j} J_{ij} \mathbf{S}_i \cdot \mathbf{S}_j - D \sum_{i,j} (\mathbf{S}_i \times \mathbf{S}_j) \cdot \mathbf{z} \\ &\quad - K \sum_i (\mathbf{S}_i \cdot \mathbf{z})^2, \end{aligned} \quad (9)$$

with the DM interaction  $-D(\mathbf{S}_i \times \mathbf{S}_j) \cdot \mathbf{z}$  oriented along bond  $i, j$  with spin  $\mathbf{S}_j$  at the end point and spin  $\mathbf{S}_i$  at the starting point of the arrow in Fig. 1. For all four models, easy-axis anisotropy  $K$  along  $\mathbf{z}$  is required to keep the DM interaction from tilting the spins away from the  $z$  axis.

In all four lattices, the DM interactions only act between sites  $r$  of the same kind in each magnetic unit cell. For the FM lattices of Figs. 1(a) and 1(c), the DM interactions act between spins of type 1 or of type 2, and similarly for the AF HC lattice in Fig. 1(b). For the AF ZZ lattice in Fig. 1(d), the DM

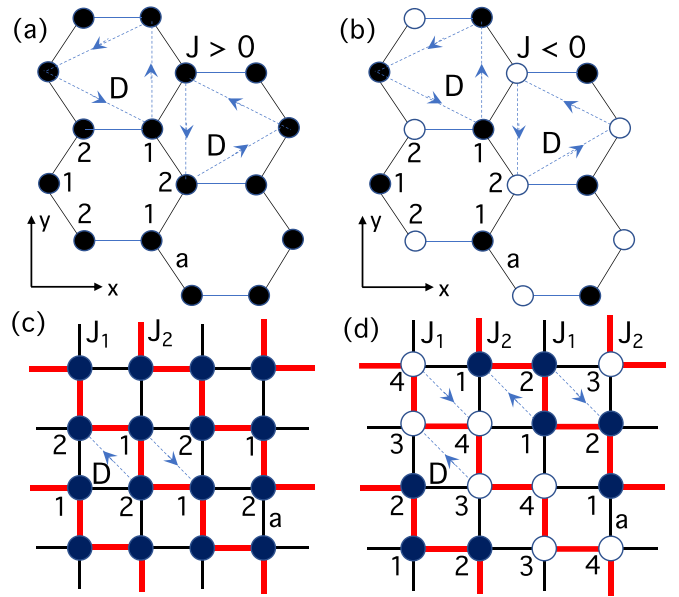


FIG. 1. Case studies: HC lattices with (a) FM interaction  $J > 0$  and (b) AF interaction  $J < 0$  with two sites in the magnetic unit cell each; ZZ lattices with (c) FM interactions  $0 < J_1 < J_2$  and two sites in the magnetic unit cell, and (d) AF interaction  $J_1 < 0$  and FM interaction  $J_2 > 0$  and four sites in the magnetic unit cell. The DM interaction  $D$  and its orientation are shown by the dashed line. Up spins are solid circles and down spins are empty circles.

interactions act between spins of type 1, 2, 3, or 4. For both HC and ZZ lattices, DM interactions are allowed by broken inversion symmetry. For the HC lattices, inversion symmetry is broken by lattice topology. For the ZZ lattices, inversion symmetry is broken by the different environment to either side of an exchange path with  $|J_2/J_1| \neq 1$ . By contrast, the environment around the midway point between neighboring spins (i.e., spins of different type) is inversion-symmetric on both lattices.

OAM was earlier predicted [27] to appear in the two ZZ lattices of Figs. 1(c) and 1(d) with  $|J_2/J_1| \neq 1$  but  $D = 0$ . Unfortunately, OAM without DM interactions cannot be observed due to its lack of gauge invariance [24]. In this paper, we find that a FM ZZ lattice with a nonzero DM interaction  $D \neq 0$  [see Fig. 1(c)] creates a new class of materials where the effects of OAM are observable. Due to the inequivalent DM interactions on either side of each bond, the FM ZZ lattice then circumvents the “no-go” theorem of Refs. [18] and [6], which is based on the edge sharing of equivalent cells. However, because the magnon bands are always degenerate along the upper left and lower right boundaries of the BZ with  $k_x - k_y = \pm\pi/a$ , the Chern numbers  $C_n$  of the magnon bands are not well defined.

The degeneracy of the FM ZZ bands along the upper left and lower right boundaries of the BZ can be lifted by allowing the FM exchange interaction  $J_n$  along the  $x$  and  $y$  axes ( $J_{nx}$  and  $J_{ny}$ ) to be slightly different. The Chern numbers of the magnon bands for the anisotropic FM ZZ model are then well defined and given by 0 or  $\pm 1$ .

There are several purposes served by this paper. The next section extends earlier results for the angular-averaged OAM

$F_n(k)$ . By studying both the FM HC and ZZ lattices, we show that formal results for  $F_n(k)$  and the Berry curvature  $\Omega_n(\mathbf{k})$  for the two models are quite similar. We also provide results for the tiling of the OAM over all  $\mathbf{k}$  for both models.

This paper is divided into six sections. Section II demonstrates that  $F_n(k)$  is the *only* component of  $O_n(k)$  that is physically observable. Section III reviews results for the FM HC model. Section IV discusses the FM ZZ model, while Sec. V treats the anisotropic model with  $J_{1y}/J_{1x} \neq 1$ . Section VI compares the predicted magnon Hall effects of the FM HC and ZZ models and contains a conclusion. To focus attention on the FM cases where OAM can be observed, we treat the AF HC and ZZ lattices in Appendixes B and C. While the FM lattices exhibit nonzero values of  $F_n(k)$  when  $D \neq 0$ , the AF lattices do not:  $F_n(k) = 0$  even when  $D \neq 0$ . Appendix D presents results for the edge modes produced by the anisotropic FM ZZ model. Because dipole interactions [13] are neglected in this paper, DM interactions provide the only source of magnon OAM.

## II. COMPONENTS OF THE OAM

To set the stage for the results provided in the next two sections, we briefly review the spin-wave (SW) formalism for the OAM and Berry curvature, specializing to collinear spin systems. Rotated into the local spin reference frame with  $\hat{\mathbf{z}}_i$  pointing along the spin direction, the spins  $\hat{\mathbf{S}}_i$  are given in terms of the boson SW creation and annihilation operators  $a_i$  and  $a_i^\dagger$  by  $\hat{S}_{iz} = S - a_i^\dagger a_i$ ,  $\hat{S}_{i+} = S_{ix}n_{iz} + iS_{iy} = \sqrt{2S}a_i$ , and  $\hat{S}_{i-} = S_{ix}n_{iz} - iS_{iy} = \sqrt{2S}a_i^\dagger$ , where  $n_{iz} = 1$  for up spins and  $n_{iz} = -1$  for down spins. Then the Hamiltonian  $H$  can be expanded in powers of the Fourier-transformed SW operators  $a_{\mathbf{k}}^{(r)}$  and  $a_{\mathbf{k}}^{(r)\dagger}$  ( $r$  is one of the  $M$  sites in the magnetic unit cell) as  $H = E_0 + H_2 + \dots$  with second-order Hamiltonian

$$H_2 = \sum_{\mathbf{k}}' \mathbf{v}_{\mathbf{k}}^\dagger \cdot \underline{L}(\mathbf{k}) \cdot \mathbf{v}_{\mathbf{k}}, \quad (10)$$

where the prime indicates that the summation over  $\mathbf{k}$  is restricted to the first BZ of the magnetic unit cell. The  $2M$ -dimensional vector operators

$$\mathbf{v}_{\mathbf{k}} = (a_{\mathbf{k}}^{(1)}, a_{\mathbf{k}}^{(2)}, \dots, a_{\mathbf{k}}^{(M)}, a_{-\mathbf{k}}^{(1)\dagger}, a_{-\mathbf{k}}^{(2)\dagger}, \dots, a_{-\mathbf{k}}^{(M)\dagger}) \quad (11)$$

satisfy  $[\mathbf{v}_{\mathbf{k}}, \mathbf{v}_{\mathbf{k}'}^\dagger] = \underline{N} \delta_{\mathbf{k}, \mathbf{k}'}$ , where  $\underline{N}$  is defined in terms of the  $M$ -dimensional identity matrix  $\underline{I}$  by

$$\underline{N} = \begin{pmatrix} \underline{I} & 0 \\ 0 & -\underline{I} \end{pmatrix}. \quad (12)$$

The  $2M \times 2M$  matrix  $\underline{L}(\mathbf{k})$  can be compactly written

$$\underline{L}(\mathbf{k}) = \begin{pmatrix} \underline{P}(\mathbf{k}) & \underline{Q}(\mathbf{k}) \\ \underline{Q}'(\mathbf{k}) & \underline{P}'(\mathbf{k}) \end{pmatrix}, \quad (13)$$

where  $\underline{P}(\mathbf{k})$ ,  $\underline{Q}(\mathbf{k})$ ,  $\underline{P}'(\mathbf{k})$ , and  $\underline{Q}'(\mathbf{k})$  are  $M \times M$  matrices. Because  $\underline{L}(\mathbf{k})$  is Hermitian,

$$\underline{P}'(\mathbf{k}) = \underline{P}(-\mathbf{k})^*, \quad (14)$$

$$\underline{Q}'(\mathbf{k}) = \underline{Q}(-\mathbf{k})^*. \quad (15)$$

These relations will prove useful in the following two sections and in Appendixes B–D.

Within the quantum SW notation, the semiclassical eigenvalue relation of Eq. (5) is replaced by

$$\underline{\Delta}(\mathbf{k}) \cdot \underline{X}^{-1}(\mathbf{k}) = \hbar \omega_n(\mathbf{k}) \underline{X}^{-1}(\mathbf{k}), \quad (16)$$

where  $\underline{\Delta}(\mathbf{k}) = \underline{N} \cdot \underline{L}(\mathbf{k})$  is non-Hermitian. Hence, the Bloch functions  $|u_n(\mathbf{k})\rangle$  are replaced by the complex matrices  $X^{-1}(\mathbf{k})_{rn}$ , which can be considered the  $n$ th eigenfunctions of the  $2M \times 2M$  energy matrix  $\underline{\Delta}(\mathbf{k})$ . In the quantum SW language, the Berry curvature and OAM are given by

$$\Omega_n(\mathbf{k}) = \frac{i}{2\pi} \sum_{r=1}^M \left\{ \frac{\partial X^{-1}(\mathbf{k})_{rn}^*}{\partial \mathbf{k}} \frac{\partial X^{-1}(\mathbf{k})_{rn}}{\partial \mathbf{k}} - \frac{\partial X^{-1}(\mathbf{k})_{r+M,n}^*}{\partial \mathbf{k}} \frac{\partial X^{-1}(\mathbf{k})_{r+M,n}}{\partial \mathbf{k}} \right\}, \quad (17)$$

$$O_n(\mathbf{k}) = \frac{\hbar}{2} \sum_{r=1}^M \{ X^{-1}(\mathbf{k})_{rn} \hat{l}_{z\mathbf{k}} X^{-1}(\mathbf{k})_{rn}^* - X^{-1}(\mathbf{k})_{r+M,n} \hat{l}_{z\mathbf{k}} X^{-1}(\mathbf{k})_{r+M,n}^* \}, \quad (18)$$

where

$$\hat{l}_{z\mathbf{k}} = -i \left( k_x \frac{\partial}{\partial k_y} - k_y \frac{\partial}{\partial k_x} \right) \quad (19)$$

is the OAM operator. The normalization condition for the Bloch functions  $\langle u_n(\mathbf{k}) | u_n(\mathbf{k}) \rangle = 1$  is then replaced by the condition

$$\sum_{r=1}^M \{ |X^{-1}(\mathbf{k})_{rn}|^2 - |X^{-1}(\mathbf{k})_{r+M,n}|^2 \} = 1 \quad (20)$$

for the complex matrices  $X^{-1}(\mathbf{k})_{rn}$  and  $X^{-1}(\mathbf{k})_{r+M,n}$ .

With the Berry curvature defined above, the Chern number for band  $n$  is given by

$$C_n = \int_{\text{BZ}} d^2k \Omega_{nz}(\mathbf{k}), \quad (21)$$

where  $\mathbf{k}$  is integrated over the first BZ [28]. A customary factor of  $1/2\pi$  is missing from this expression for  $C_n$  because it is included in Eqs. (1) and (17) for the Berry phases. The Chern number  $C_n$  takes an integer value as long as the magnons in band  $n$  are nondegenerate, i.e., disconnected from all other magnons in frequency for all  $\mathbf{k}$ . A nonzero Chern number is physically associated with edge modes [19,20,29–31] whose dispersion bridges the gap between bulk magnon bands. Since the sum of Berry curvatures over all bands vanishes,  $\sum_n C_n = 0$ .

In the quantum language, each eigenfunction  $X^{-1}(\mathbf{k})_{rn}$  can be multiplied by an arbitrary phase factor so that

$$X^{-1}(\mathbf{k})_{rn} \rightarrow X^{-1}(\mathbf{k})_{rn} e^{-i\lambda_n(\mathbf{k})}, \quad (22)$$

where the gauge  $\lambda_n(\mathbf{k})$  may depend on band index  $n$  and  $\mathbf{k} = (k, \phi)$  but not on site  $r$ . Of course,  $\lambda_n(k, \phi)$  must also be a single-valued function of  $\phi$  so that  $\lambda_n(k, 0) = \lambda_n(k, 2\pi)$ . Under a gauge transformation, the OAM changes by

$$O_n(\mathbf{k}) \rightarrow O_n(\mathbf{k}) + \frac{\hbar}{2} \frac{\partial}{\partial \phi} \lambda_n(k, \phi), \quad (23)$$

in agreement with the semiclassical expression of Eq. (7).

Now expand  $O_n(k, \phi)$  in powers of  $\cos l\phi$  and  $\sin l\phi$  so that

$$O_n(k, \phi) = \sum_{l=0} \{A_{ln}(k) \cos l\phi + B_{ln}(k) \sin l\phi\}. \quad (24)$$

Following a gauge transformation, the right-hand side (rhs) of Eq. (23) becomes

$$\begin{aligned} & \sum_{l=0} \{A_{ln}(k) \cos l\phi + B_{ln}(k) \sin l\phi\} + \frac{\hbar}{2} \frac{\partial}{\partial \phi} \lambda_n(k, \phi) \\ &= A_{0n}(k) + \sum_{l=1} \{A_{ln}(k) \cos l\phi + B_{ln}(k) \sin l\phi\} \\ &+ \frac{\hbar}{2} \frac{\partial}{\partial \phi} \lambda_n(k, \phi) = A_{0n}(k), \end{aligned} \quad (25)$$

where we have set

$$\begin{aligned} \lambda_n(k, \phi) = & -\frac{2}{\hbar} \sum_{l=1} \frac{1}{l} \{A_{ln}(k) \sin l\phi \\ & - B_{ln}(k) \cos l\phi\}. \end{aligned} \quad (26)$$

The  $l = 0$  component cannot be included on the rhs because it would produce a term proportional to  $\phi$ , violating the assumption that  $\lambda_n(k, 0) = \lambda_n(k, 2\pi)$ . Hence, the appropriate gauge  $\lambda_n(k)$  can be used to remove all components of the OAM except for

$$A_{0n}(k) = F_n(k) \equiv \int_0^{2\pi} \frac{d\phi}{2\pi} O_n(\mathbf{k}). \quad (27)$$

Not only does this prove that  $F_n(k)$  is observable, but it also demonstrates that  $F_n(k)$  is the *only* observable component of the OAM.

In the absence of DM interactions, the OAM  $O_n(\mathbf{k})$  is an odd function of  $\mathbf{k}$  so that  $O_n(\mathbf{k}) = -O_n(-\mathbf{k})$  and  $F_n(k) = 0$ . When the DM interaction  $D$  enters  $O_n(\mathbf{k})$  linearly, then  $O_n(\mathbf{k}) = O_n(-\mathbf{k})$  is an even function of  $\mathbf{k}$ , and  $F_n(k)$  can be nonzero. More generally, we expand  $O_n(\mathbf{k})$  in powers of the DM interaction as

$$\begin{aligned} O_n(\mathbf{k}) = & O_n^{(0)}(\mathbf{k}) + D O_n^{(1)}(\mathbf{k}) + D^2 O_n^{(2)}(\mathbf{k}) \\ & + D^3 O_n^{(3)}(\mathbf{k}) + \dots \end{aligned} \quad (28)$$

Then, the even components  $O_n^{(2m)}(\mathbf{k}) = -O_n^{(2m)}(-\mathbf{k})$  are odd in  $\mathbf{k}$  and the odd components  $O_n^{(2m+1)}(\mathbf{k}) = O_n^{(2m+1)}(-\mathbf{k})$  are even in  $\mathbf{k}$ . Of course, only the odd components  $O_n^{(2m+1)}(\mathbf{k})$  contribute to  $F_n(k)$ . If we then write

$$O_n(\mathbf{k}) = O_n^{(\text{odd})}(\mathbf{k}) + O_n^{(\text{even})}(\mathbf{k}), \quad (29)$$

only  $O_n^{(\text{even})}(\mathbf{k})$  (containing terms of order  $D^{2m+1}$ ) contributes to the physically measurable  $F_n(k)$ .

Since only wave vectors  $\mathbf{k}$  within the first BZ of the magnetic unit cell enter Eq. (10), we use periodic boundary conditions to evaluate the integral over angles  $\phi$  in  $F_n(k)$  when required to translate wave vectors  $\mathbf{k}$  outside the first BZ to wave vectors inside the first BZ. Alternatively,  $F_n(k)$  can be evaluated by tiling all of  $\mathbf{k}$  space with the first BZ of  $O_n^{(\text{even})}(\mathbf{k})$ . For the FM ZZ lattice, Appendix A shows that the resulting pattern for  $O_n^{(\text{tilled})}(\mathbf{k})$  is both periodic in  $\mathbf{k}$  and continuous as a function of  $\mathbf{k}$  at the zone boundaries. We shall give examples of the tiling procedure for the FM HC and ZZ models in the following sections. Nevertheless, bear in mind

that  $O_n^{(\text{tilled})}(\mathbf{k})$  is not unique and is just a tool to evaluate the physically observable quantity  $F_n(k)$ .

### III. FM HONEYCOMB LATTICE

Most details of the solution for the FM HC lattice sketched in Fig. 1(a) with exchange  $J > 0$  and DM interaction  $D$  between like sites were previously provided in Ref. [24]. The  $4 \times 4$  matrix  $\underline{L}(\mathbf{k})$  defined by Eq. (10) is given by

$$\underline{L}(\mathbf{k}) = \frac{3JS}{2} \begin{pmatrix} A_{\mathbf{k}}^- & -\Gamma_{\mathbf{k}}^* & 0 & 0 \\ -\Gamma_{\mathbf{k}} & A_{\mathbf{k}}^+ & 0 & 0 \\ 0 & 0 & A_{\mathbf{k}}^+ & -\Gamma_{\mathbf{k}}^* \\ 0 & 0 & -\Gamma_{\mathbf{k}} & A_{\mathbf{k}}^- \end{pmatrix}, \quad (30)$$

where  $A_{\mathbf{k}}^{\pm} = 1 \pm d \Theta_{\mathbf{k}} + \kappa$ ,  $d = -2D/3J$ ,  $\kappa = 2K/3J$ ,

$$\Theta_{\mathbf{k}} = 4 \cos(3k_x a/2) \sin(\sqrt{3}k_y a/2) - 2 \sin(\sqrt{3}k_y a), \quad (31)$$

and

$$\Gamma_{\mathbf{k}} = \frac{1}{3} \{e^{ik_x a} + 2e^{-ik_x a/2} \cos(\sqrt{3}k_y a/2)\}. \quad (32)$$

We caution the reader that matrix element  $A_{\mathbf{k}}^{\pm}$ , DM parameter  $d$ , and anisotropy parameter  $\kappa$  shall be defined differently for the FM ZZ lattice in the next section. Since  $\Theta_{-\mathbf{k}} = -\Theta_{\mathbf{k}}$  and  $\Gamma_{-\mathbf{k}} = \Gamma_{\mathbf{k}}^*$ , it can be easily shown that the upper and lower quadrants of  $\underline{L}(\mathbf{k})$  satisfy Eq. (14) or that  $\underline{P}'(\mathbf{k}) = \underline{P}(-\mathbf{k})^*$ .

Magnon energies for bands 1 and 2 are given by

$$\hbar\omega_1(\mathbf{k}) = 3JS(1 - \eta_{\mathbf{k}} + \kappa), \quad (33)$$

$$\hbar\omega_2(\mathbf{k}) = 3JS(1 + \eta_{\mathbf{k}} + \kappa), \quad (34)$$

where  $\eta_{\mathbf{k}} = \sqrt{|\Gamma_{\mathbf{k}}|^2 + (d \Theta_{\mathbf{k}})^2}$ . Notice that these energies are simply shifted by the easy-axis anisotropy  $\kappa$ . The magnon band gap is given by

$$\hbar\Delta\omega(\mathbf{k}) = \hbar[\omega_2(\mathbf{k}) - \omega_1(\mathbf{k})] = 6JS\eta_{\mathbf{k}}. \quad (35)$$

The normalized gap

$$\delta(\mathbf{k}) \equiv \frac{\hbar\Delta\omega(\mathbf{k})}{6JS} = 2\eta_{\mathbf{k}} = 2\sqrt{|\Gamma_{\mathbf{k}}|^2 + (d \Theta_{\mathbf{k}})^2} \quad (36)$$

is plotted versus  $\mathbf{k}$  for  $d = 0$  and  $-0.4$  in Fig. 2. When  $d = 0$ , the magnon gap vanishes in triangular  $\mathbf{k}$ -space regions at the corners of the BZ. When  $d = -0.4$ , the smallest normalized gap  $\delta(\mathbf{k})$  is  $2/3$ . In fact, any nonzero  $d$  introduces a gap such that the  $\delta(\mathbf{k}) > 0$  and modes 1 and 2 are distinct for all  $\mathbf{k}$ .

Using a particularly simple form for the gauge, we earlier found [24] (correcting a minus sign) that

$$O_1(\mathbf{k}) = \frac{\hbar}{4} \left\{ 1 - \frac{d \Theta_{\mathbf{k}}}{\eta_{\mathbf{k}}} \right\} \frac{\Gamma_{\mathbf{k}}}{|\Gamma_{\mathbf{k}}|} \hat{t}_{z\mathbf{k}} \frac{\Gamma_{\mathbf{k}}^*}{|\Gamma_{\mathbf{k}}|}, \quad (37)$$

$$O_2(\mathbf{k}) = \frac{\hbar}{4} \left\{ 1 + \frac{d \Theta_{\mathbf{k}}}{\eta_{\mathbf{k}}} \right\} \frac{\Gamma_{\mathbf{k}}}{|\Gamma_{\mathbf{k}}|} \hat{t}_{z\mathbf{k}} \frac{\Gamma_{\mathbf{k}}^*}{|\Gamma_{\mathbf{k}}|}. \quad (38)$$

Unlike the mode frequencies, however, solutions for the OAM are not unique. Since the  $d = 0$  portion of the OAM is not observable, the first terms in the brackets of Eqs. (37) and (38) can be neglected. Because  $\eta_{\mathbf{k}}$  is an even function of  $d$ , we then find

$$O_1^{(\text{even})}(\mathbf{k}) = -O_2^{(\text{even})}(\mathbf{k}) = -\frac{d \hbar \Theta_{\mathbf{k}}}{4} \frac{\Gamma_{\mathbf{k}}}{\eta_{\mathbf{k}} |\Gamma_{\mathbf{k}}|} \hat{t}_{z\mathbf{k}} \frac{\Gamma_{\mathbf{k}}^*}{|\Gamma_{\mathbf{k}}|} \quad (39)$$

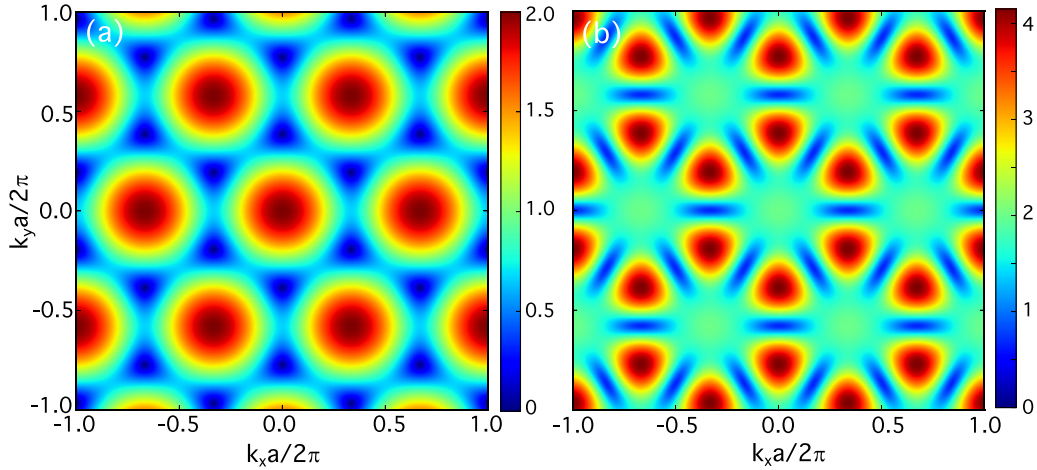


FIG. 2. The normalized gap  $\delta(\mathbf{k}) = 2\eta_{\mathbf{k}}$  for the FM HC lattice vs  $\mathbf{k}$  for  $d =$  (a) 0 and (b)  $-0.4$ .

and

$$F_1(k) = -F_2(k) = -\frac{d\hbar}{4} \int \frac{d\phi}{2\pi} \frac{\Theta_{\mathbf{k}}}{\eta_{\mathbf{k}}} \frac{\Gamma_{\mathbf{k}}}{|\Gamma_{\mathbf{k}}|} \hat{l}_{z\mathbf{k}} \frac{\Gamma_{\mathbf{k}}^*}{|\Gamma_{\mathbf{k}}|}. \quad (40)$$

Figure 3 uses  $O_1^{(\text{even})}(\mathbf{k})/\hbar$  with  $d = -0.1$  to construct  $O_1^{(\text{tiled})}(\mathbf{k})/\hbar$ . Notice that the tiled pattern is both a periodic function of  $\mathbf{k}$  and a continuous function of  $\mathbf{k}$  at the boundaries of the first BZ, denoted by the solid lines. The solutions for  $F_1(k)/\hbar$  for  $d$  running from  $-0.01$  to  $-0.1$  are plotted in Fig. 4. We find that  $F_1(k)/\hbar$  grows quite rapidly with  $d$  and peaks when  $ka/2\pi = 2\sqrt{3}/9 = 0.385$ , which coincides with the corners of the first BZ. The value of  $F_1(k)/\hbar$  at  $ka/2\pi = 2\sqrt{3}/9$  diverges as  $|d| \rightarrow \infty$ .

While Fig. 3 suggests that the OAM is largest at the corners of the BZ and Fig. 4 does not disallow that claim, we remind the reader that Fig. 4 only states that the angular average of the OAM is largest when  $ka/2\pi$  intercepts the corners of the BZ. It does *not* imply that the largest OAM lies for  $\phi$  at the BZ corners.

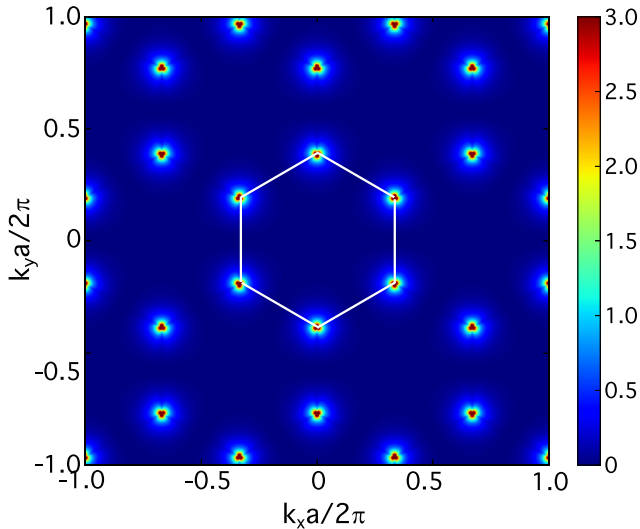


FIG. 3. The pattern  $O_1^{(\text{tiled})}(\mathbf{k})/\hbar$  for the FM HC lattice with  $d = -0.1$ . The first BZ of the magnetic unit cell is denoted by the solid white lines.

Again correcting a minus sign, the Berry curvatures of the FM HC lattice are given analytically by

$$\begin{aligned} \Omega_{1z}(\mathbf{k}) &= -\Omega_{2z}(\mathbf{k}) \\ &= i \frac{d}{4\pi} \frac{\Gamma_{\mathbf{k}}^*}{|\Gamma_{\mathbf{k}}|} \left\{ \frac{\partial \Theta_{\mathbf{k}}/\eta_{\mathbf{k}}}{\partial \mathbf{k}} \times \frac{\partial \Gamma_{\mathbf{k}}/|\Gamma_{\mathbf{k}}|}{\partial \mathbf{k}} \right\} \cdot \mathbf{z}. \end{aligned} \quad (41)$$

For the lower band,  $\Omega_{1z}(\mathbf{k})$  is plotted in Fig. 5 for  $d = -0.1$  and  $-0.4$ . The Chern numbers  $C_n$  of the lower and upper magnon bands are  $-1$  and  $+1$ , respectively, for all  $d < 0$ . The Chern number is an integer due to the nonzero gap [28] between the magnon modes for all  $\mathbf{k}$ .

#### IV. FM ZIGZAG LATTICE

The FM ZZ lattice is sketched in Fig. 1(c) with exchange interactions  $0 < J_1 < J_2$  and DM interaction  $D$  between like

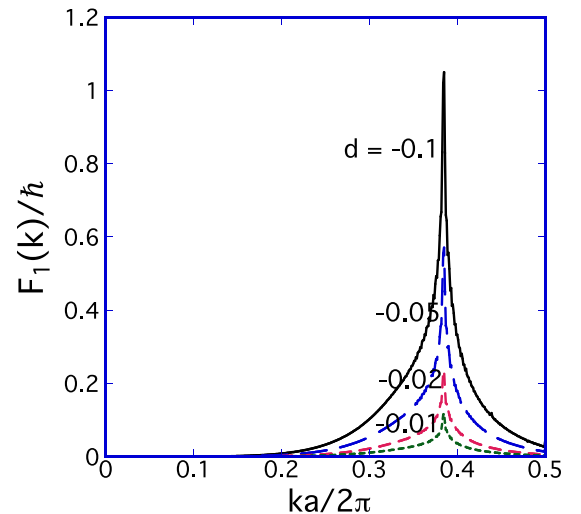


FIG. 4. The function  $F_1(k)/\hbar$  evaluated using  $O_1^{(\text{tiled})}(\mathbf{k})/\hbar$  for the FM HC lattice with  $d = -0.01, -0.02, -0.05,$  and  $-0.1$ .

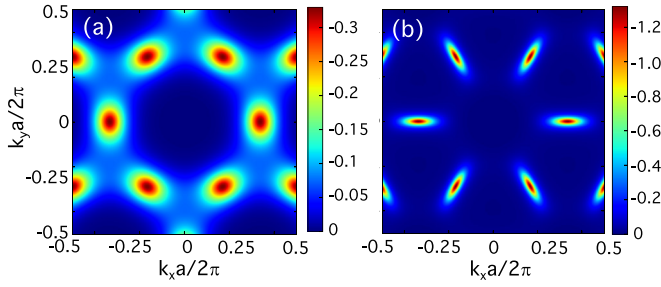


FIG. 5. The Berry curvature  $\Omega_{1z}(\mathbf{k})$  of the FM HC lattice vs  $\mathbf{k}$  for  $d =$  (a)  $-0.1$  and (b)  $-0.4$ .

sites along  $(1, -1)$ . Then

$$\underline{L}(\mathbf{k}) = (J_1 + J_2)S \begin{pmatrix} A_{\mathbf{k}}^- & -\Psi_{\mathbf{k}}^* & 0 & 0 \\ -\Psi_{\mathbf{k}} & A_{\mathbf{k}}^+ & 0 & 0 \\ 0 & 0 & A_{\mathbf{k}}^+ & -\Psi_{\mathbf{k}}^* \\ 0 & 0 & -\Psi_{\mathbf{k}} & A_{\mathbf{k}}^- \end{pmatrix}, \quad (42)$$

where  $A_{\mathbf{k}}^{\pm} = 1 \pm d \tau_{\mathbf{k}} + \kappa$ ,  $d = -2D/(J_1 + J_2)$ ,  $\kappa = K/(J_1 + J_2)$ ,  $\tau_{\mathbf{k}} = \sin(k_y a - k_x a)$ , and

$$\Psi_{\mathbf{k}} = \frac{J_1 \xi_{\mathbf{k}}^* + J_2 \xi_{\mathbf{k}}}{2(J_1 + J_2)} \quad (43)$$

with  $\xi_{\mathbf{k}} = \exp(ik_x a) + \exp(ik_y a)$ . Using  $\tau_{-\mathbf{k}} = -\tau_{\mathbf{k}}$  and  $\Psi_{-\mathbf{k}} = \Psi_{\mathbf{k}}^*$ , it is easy to verify that the upper and lower quadrants of  $\underline{L}(\mathbf{k})$  satisfy Eq. (14) or that  $\underline{P}'(\mathbf{k}) = \underline{P}'(-\mathbf{k})^*$ .

The magnon energies are given by

$$\hbar\omega_1(\mathbf{k}) = 2(J_1 + J_2)S(1 - \mu_{\mathbf{k}} + \kappa), \quad (44)$$

$$\hbar\omega_2(\mathbf{k}) = 2(J_1 + J_2)S(1 + \mu_{\mathbf{k}} + \kappa), \quad (45)$$

where  $\mu_{\mathbf{k}} = \sqrt{|\Psi_{\mathbf{k}}|^2 + (d \tau_{\mathbf{k}})^2}$ . As for the FM HC lattice, the magnon bands are just shifted by  $\kappa$ . The gap between the magnons is then given by

$$\hbar\Delta\omega(\mathbf{k}) = \hbar[\omega_2(\mathbf{k}) - \omega_1(\mathbf{k})] = 4(J_1 + J_2)S\mu_{\mathbf{k}}, \quad (46)$$

with a normalized gap

$$\delta(\mathbf{k}) \equiv \frac{\hbar\Delta\omega(\mathbf{k})}{2(J_1 + J_2)S} = 2\mu_{\mathbf{k}} = 2\sqrt{|\Psi_{\mathbf{k}}|^2 + (d \tau_{\mathbf{k}})^2} \quad (47)$$

that only depends on  $d$  and  $r = J_2/J_1$ . The normalized gap is plotted versus  $\mathbf{k}$  on the top two panels of Fig. 6 for  $d = 0$  and  $r = 8$  or  $1$ . For  $r > 1$ ,  $\delta(\mathbf{k}) = 0$  at the upper left and lower right borders of the BZ, which is sketched by the rotated square. For  $r = 1$ ,  $\delta(\mathbf{k}) = 0$  at all four borders of the BZ. The bottom two panels of Fig. 6 plot  $\delta(\mathbf{k})$  for the same values of  $r$  with  $d = -0.4$ . Even for  $d \neq 0$ , the gap  $\delta(\mathbf{k})$  continues to vanish at the upper left and lower right boundaries of the BZ with  $k_x - k_y = \pm\pi/a$  because  $\tau_{\mathbf{k}} = 0$ .

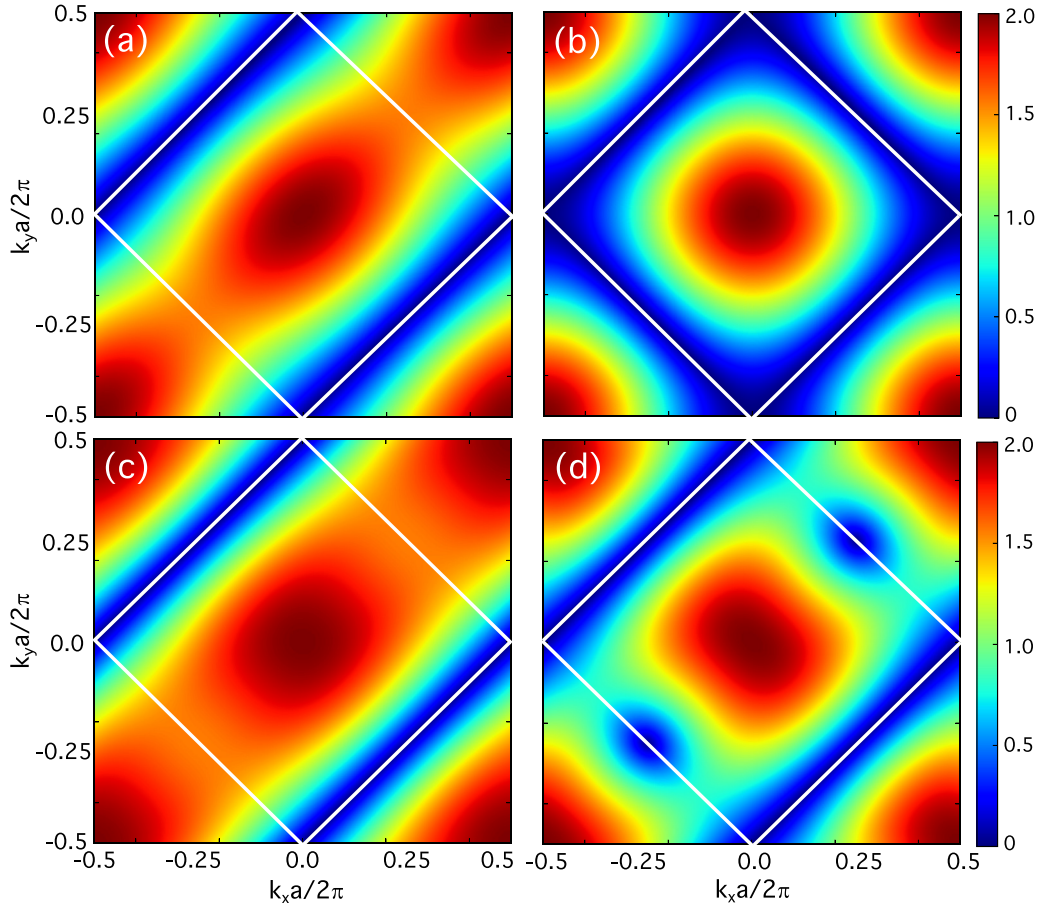


FIG. 6. The normalized gap  $\delta(\mathbf{k}) = 2\mu_{\mathbf{k}}$  between bands of the FM ZZ lattice evaluated using  $d = 0$  and  $r =$  (a)  $8$  and (b)  $1$  in the top two panels or  $d = -0.4$  and  $r =$  (c)  $8$  and (d)  $1$  in the bottom two panels. The first BZ of the magnetic unit cell is sketched by the solid lines.

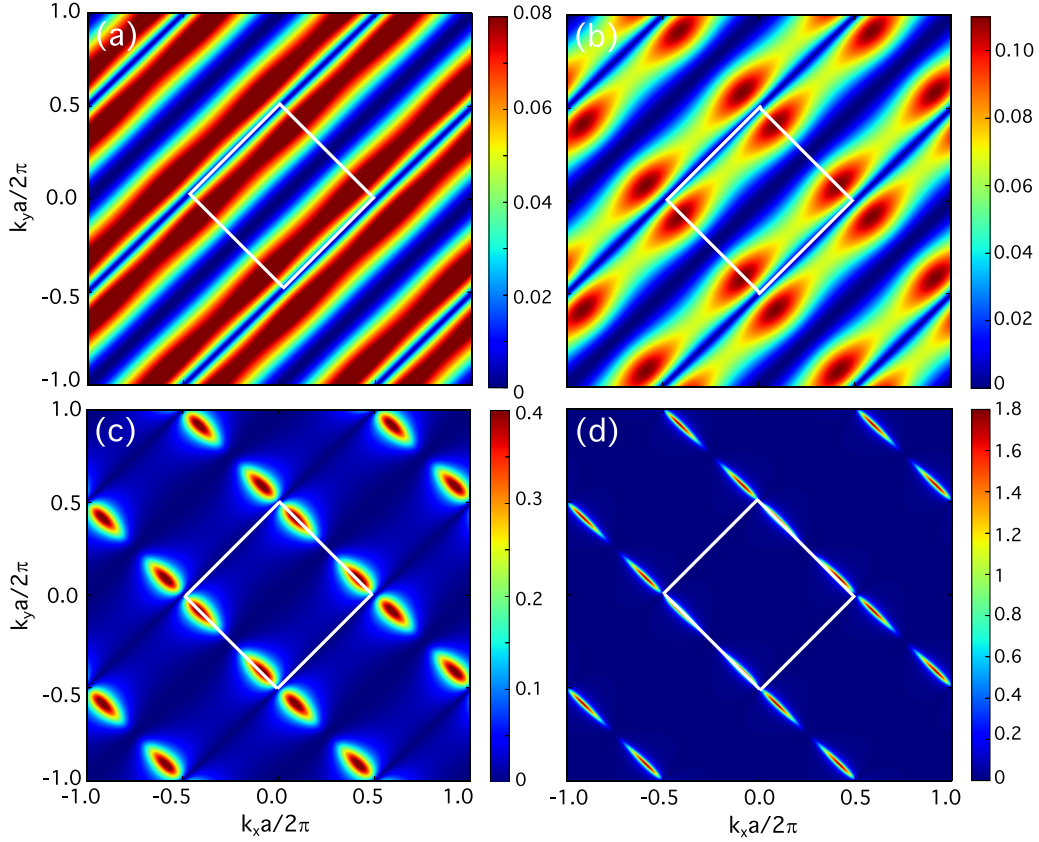


FIG. 7. The pattern  $O_1^{(\text{tiled})}(\mathbf{k})/\hbar$  for the FM ZZ lattice with  $d = -0.4$  and  $r =$  (a) 50, (b) 8, (c) 1.5, and (d) 1.1. The first BZ of the magnetic unit cell is denoted by the solid white lines.

The solutions for  $O_n^{(\text{even})}(\mathbf{k})$  and  $F_n(k)$  are formally quite similar to those for the FM HC lattice in Eqs. (39) and (40):

$$O_1^{(\text{even})}(\mathbf{k}) = -O_2^{(\text{even})}(\mathbf{k}) = -\frac{d\hbar}{4} \frac{\tau_{\mathbf{k}}}{\mu_{\mathbf{k}}} \frac{\Psi_{\mathbf{k}}}{|\Psi_{\mathbf{k}}|} \hat{l}_{z\mathbf{k}} \frac{\Psi_{\mathbf{k}}^*}{|\Psi_{\mathbf{k}}|} \quad (48)$$

and

$$F_1(k) = -F_2(k) = -\frac{d\hbar}{4} \int \frac{d\phi}{2\pi} \frac{\tau_{\mathbf{k}}}{\mu_{\mathbf{k}}} \frac{\Psi_{\mathbf{k}}}{|\Psi_{\mathbf{k}}|} \hat{l}_{z\mathbf{k}} \frac{\Psi_{\mathbf{k}}^*}{|\Psi_{\mathbf{k}}|}. \quad (49)$$

The pattern  $O_1^{(\text{tiled})}(\mathbf{k})/\hbar$  is plotted in Fig. 7 for  $d = -0.4$  and  $r = 50, 8, 1.5,$  and  $1.1$ . For  $r = 50$  or  $8$ ,  $O_1^{(\text{tiled})}(\mathbf{k})/\hbar$  contains wide troughs of minima close to zero near avenues of maxima close to  $0.08$  or  $0.11\hbar$ , both along  $(1,1)$ . Narrow lanes of vanishing OAM appear at the  $k_x - k_y = \pm\pi/a$  boundaries of the BZ where the magnon bands are degenerate. The OAM also vanishes in a lane along  $(1,1)$  that crosses  $\mathbf{k} = 0$ . For  $r = 1.5$  and  $1.1$ , peaked regions in  $O_1^{(\text{tiled})}(\mathbf{k})/\hbar$  appear at the  $k_x + k_y = \pm\pi/a$  boundaries of the BZ along  $(1, -1)$ . These regions become increasingly narrow as  $r \rightarrow 1$ .

The observable function  $F_n(k)/\hbar$  for the FM ZZ lattice is plotted in Fig. 8 for  $d = -0.4$  and these same four values of  $r$ . For  $r = 1.5$  and  $1.1$ , the large maxima of  $F_1(k)/\hbar$  at  $ka/2\pi \approx 0.4$  are associated with the peaked regions of  $O_1^{(\text{tiled})}(\mathbf{k})/\hbar$  at the lower left and upper right boundaries of the

BZ ( $k_x + k_y = \pm\pi/a$ ) in Fig. 7. The observable portion of the OAM becomes increasingly narrow and disappears as  $r \rightarrow 1$ .

Since the magnon Hall effect may be observed in the FM ZZ lattice with DM interaction, we also provide results for its Berry curvature. The Berry curvatures along  $z$  may be written

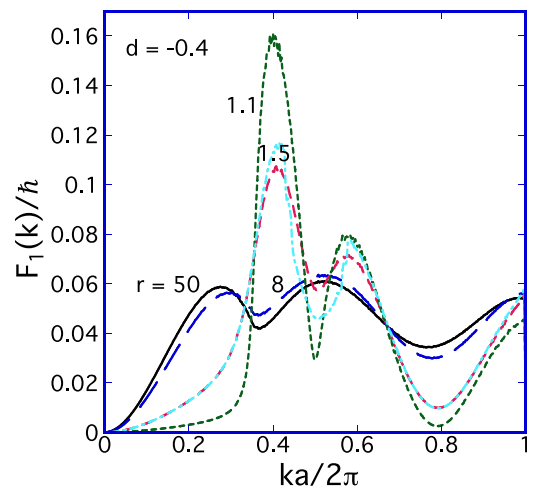


FIG. 8. The function  $F_1(k)/\hbar$  evaluated using  $O_1^{(\text{tiled})}(\mathbf{k})/\hbar$  for the FM ZZ lattice with  $d = -0.4$  and  $r = 50, 8, 1.5$  (long-dash curve), and  $1.1$ . The short-dash curve for  $r = 1.5$  takes  $J_{1y}/J_{1x} = 1.1$  in the anisotropic ZZ model.

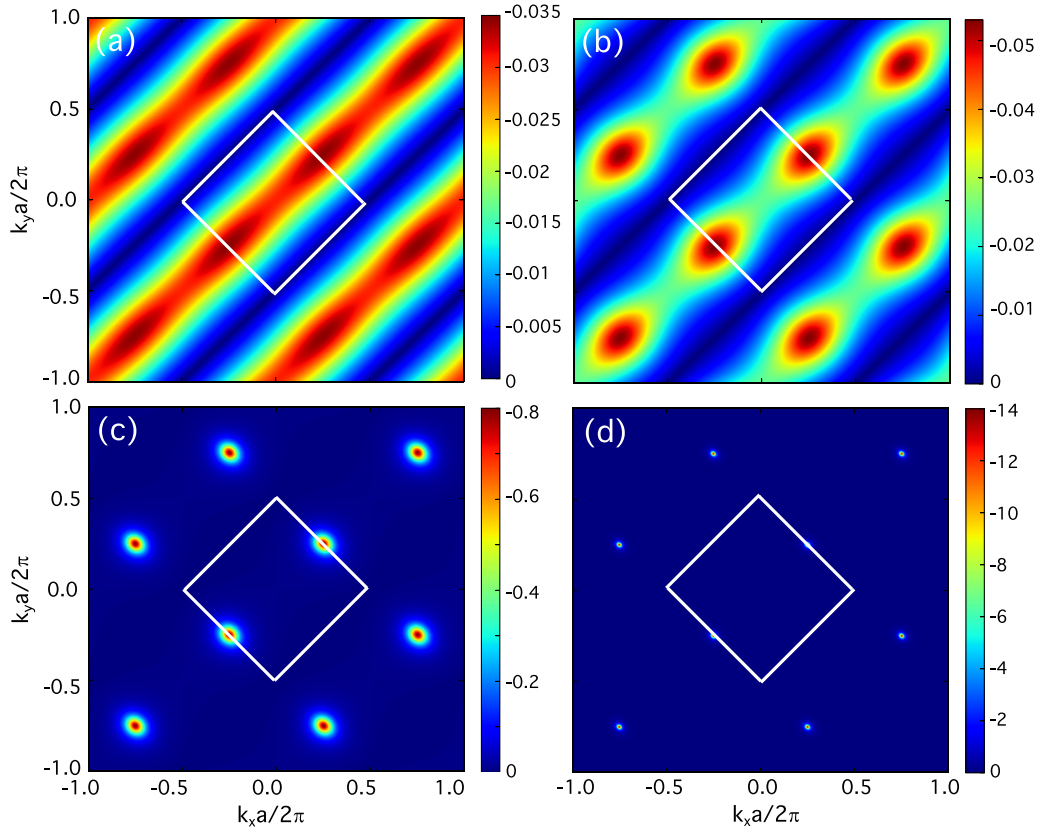


FIG. 9. The Berry curvature  $\Omega_{1z}(\mathbf{k})$  of the FM ZZ lattice evaluated using  $d = -0.4$  and  $r =$  (a) 50, (b) 8, (c) 1.5, and (d) 1.1. The first BZ of the magnetic unit cell is sketched by the solid lines.

as

$$\begin{aligned} \Omega_{1z}(\mathbf{k}) &= -\Omega_{2z}(\mathbf{k}) \\ &= i \frac{d}{4\pi} \frac{\Psi_{\mathbf{k}}^*}{|\Psi_{\mathbf{k}}|} \left\{ \frac{\partial \tau_{\mathbf{k}}/\mu_{\mathbf{k}}}{\partial \mathbf{k}} \times \frac{\partial \Psi_{\mathbf{k}}/|\Psi_{\mathbf{k}}|}{\partial \mathbf{k}} \right\} \cdot \mathbf{z}, \end{aligned} \quad (50)$$

which are formally similar to the expressions for the Berry curvatures of the FM HC lattice given by Eq. (41). Using the same parameters as in Figs. 7 and 8, we plot  $\Omega_{1z}(\mathbf{k})$  in Fig. 9.

Comparing Figs. 6 and 9 reveals that the Berry curvature vanishes at the upper left and lower right boundaries of the BZ with  $k_x - k_y = \pm\pi/a$ , where the magnon gap  $\delta(\mathbf{k})$  also vanishes. For any  $r$ , the DM interaction does not affect the gap at  $k_x = k_y = \pm 0.5\pi/a$ , where  $\tau_{\mathbf{k}} = 0$  and  $\delta(\mathbf{k}) = 2|\Psi_{\mathbf{k}}| = 2|1 - r|/(1 + r)$ . So at  $r = 1$ , the gap between the bands closes at those two points. Close to  $r = 1$ , strong peaks in the Berry curvature are found at those same  $\mathbf{k}$  points in Fig. 9. However, the Berry curvature disappears when the exchange becomes homogeneous as  $r \rightarrow 1$ .

Evaluating the Chern number  $C_n$  for the FM ZZ model by integrating  $\Omega_{nz}(\mathbf{k})$  over all  $\mathbf{k}$  within the first BZ zone, we obtain the surprising result that  $C_n$  is not well defined. Recall that the Chern numbers for the FM HC lattice are  $\pm 1$  for all  $d$ . The Chern numbers for the FM ZZ model are not well defined due to the degeneracy of the magnon bands at the upper right and lower left boundaries of the BZ.

## V. ANISOTROPIC FM ZIGZAG LATTICE

As mentioned earlier, the degeneracy of the magnon bands along the BZ boundaries can be lifted by allowing the exchanges  $J_{nx}$  along the  $x$  axis to be different from the exchanges  $J_{ny}$  along the  $y$  axis. Earlier results must then be modified by defining  $J_t = J_{1x} + J_{1y} + J_{2x} + J_{2y}$ ,  $d = -4D/J_t$ ,

$$\Psi_{\mathbf{k}} = \frac{J_{1x}e^{-ik_x a} + J_{1y}e^{-ik_y a} + J_{2x}e^{ik_x a} + J_{2y}e^{ik_y a}}{J_t}, \quad (51)$$

$$\hbar\omega_1(\mathbf{k}) = J_t S(1 - \mu_{\mathbf{k}} + \kappa), \quad (52)$$

$$\hbar\omega_2(\mathbf{k}) = J_t S(1 + \mu_{\mathbf{k}} + \kappa), \quad (53)$$

$$r = \frac{J_{2x} + J_{2y}}{J_{1x} + J_{1y}} > 1, \quad (54)$$

and  $\delta(\mathbf{k}) = \hbar\Delta\omega(\mathbf{k})/J_t S$ .

The anisotropic FM ZZ model contains three regimes depending on the relative values of  $\Delta J_1 = |J_{1y} - J_{1x}|$  and  $\Delta J_2 = |J_{2y} - J_{2x}|$ , with the constraint that  $r > 1$ . For the case  $\Delta J_1 = \Delta J_2 = 0$  considered in the previous section, the Chern number is undefined and the gap between the bands vanishes even when  $d \neq 0$ . The Chern number remains undefined when  $\Delta J_1 = \Delta J_2 > 0$ , although the gap between the bands is then nonzero due to the exchange anisotropy in the  $x$  and  $y$  directions. For  $\Delta J_1 > \Delta J_2 \geq 0$ , the Chern numbers  $C_n$  for the lower and upper bands are  $-1$  and  $+1$  when  $d < 0$  and reversed when  $d > 0$ . When



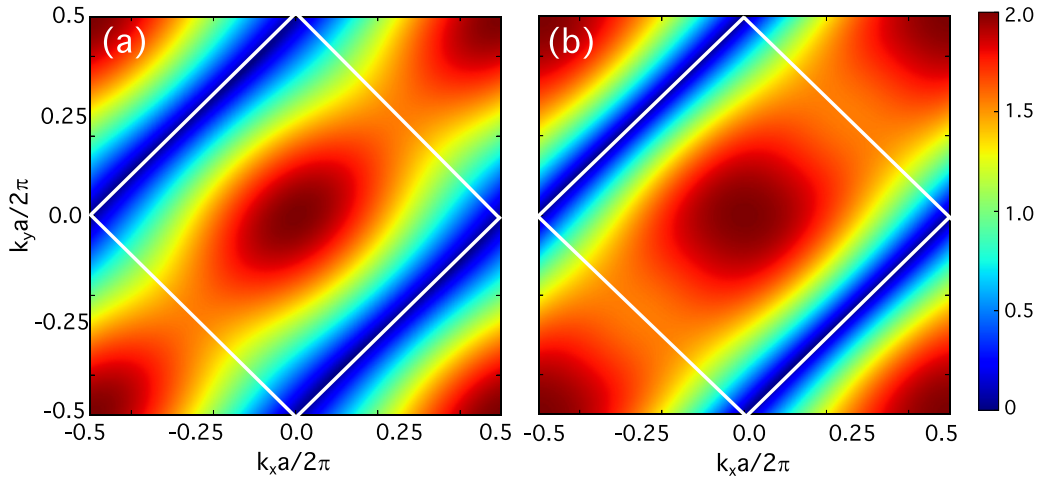


FIG. 10. The normalized gap  $\delta(\mathbf{k}) = 2\mu_{\mathbf{k}}$  between bands of the FM ZZ lattice evaluated using  $J_{1y}/J_{1x} = 1.5$ ,  $\Delta J_2 = 0$ ,  $r = 8$ , and (a)  $d = 0$  or (b)  $-0.4$ . The first BZ of the magnetic unit cell is sketched by the solid lines.

$\Delta J_2 > \Delta J_1 \geq 0$ ,  $C_n = 0$ . Consequently, the anisotropic FM ZZ model bears some similarity to the Su-Schrieffer-Heeger model [32].

For simplicity, we now consider the case in which  $\Delta J_1 \neq 0$  but  $\Delta J_2 = 0$ . Using  $J_{1y}/J_{1x} = 1.5$ , the normalized gap  $\delta(\mathbf{k})$  is plotted versus  $\mathbf{k}$  in Fig. 10. The minimum value of  $\delta(\mathbf{k})$  increases from  $2.9 \times 10^{-3}$  to  $2.5 \times 10^{-2}$  as  $|d|$  increases from 0 to 0.4. The short-dash curve in Fig. 8 for  $r = 1.5$  uses

$J_{1y}/J_{1x} = 1.1$ , indicating a redistribution of OAM to values of  $k$  near its peak.

The Berry curvatures of the anisotropic FM ZZ model with  $J_{1y}/J_{1x} = 1.5$ ,  $\Delta J_2 = 0$ , and  $d = -0.4$  are plotted in Fig. 11 for four different values of  $r$ . Notice that the range of Berry curvatures now extends over both positive and negative values with the upper negative bounds for  $d = -0.4$  exceeding the range for  $J_{1y}/J_{1x} = 1$  in Fig. 9. These negative

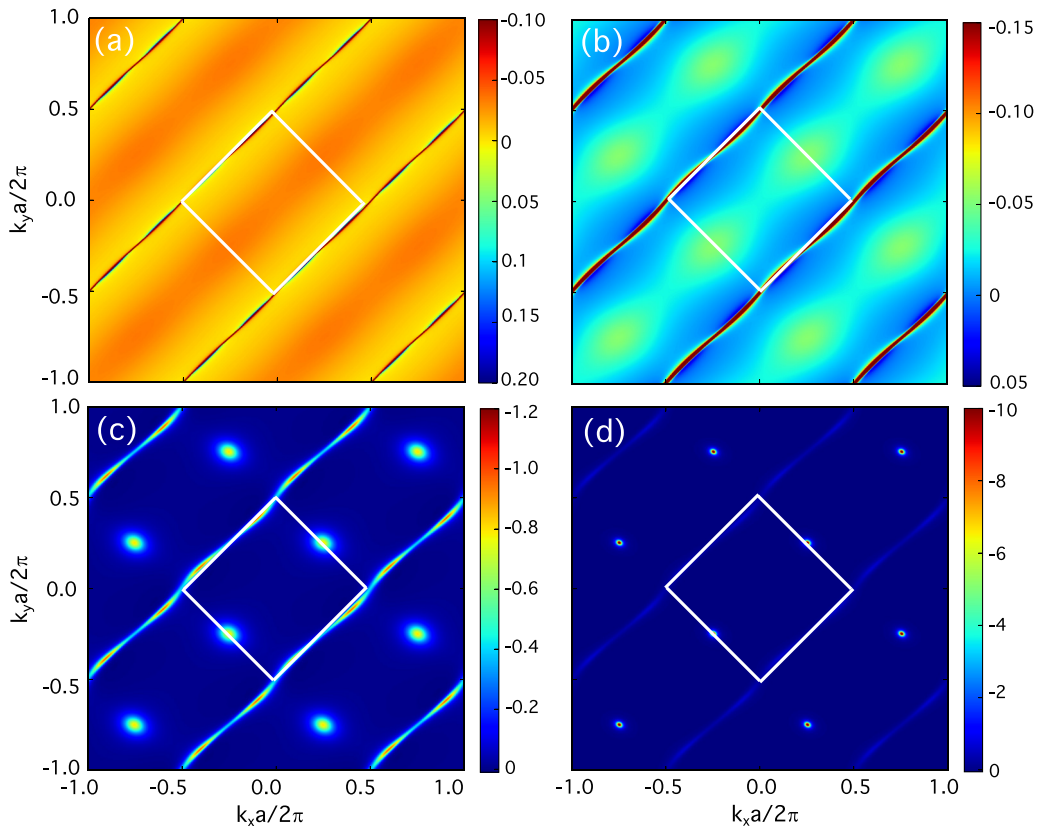


FIG. 11. The Berry curvature  $\Omega_{1z}(\mathbf{k})$  of the FM ZZ lattice evaluated using  $d = -0.4$ ,  $J_{1y}/J_{1x} = 1.5$ ,  $\Delta J_2 = 0$ , and  $r =$  (a) 50, (b) 8, (c) 1.5, and (d) 1.1. The first BZ of the magnetic unit cell is sketched by the solid lines.

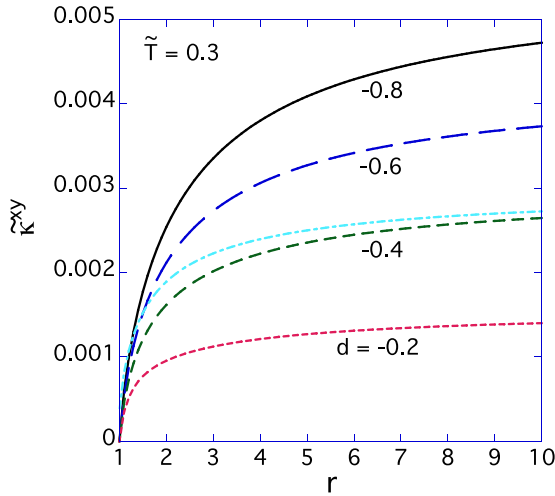


FIG. 12. The normalized thermal conductivity  $\tilde{\kappa}^{xy}(\tilde{T})$  vs  $r$  for several values of  $d$  for the FM ZZ model with temperature  $\tilde{T} = 0.3$  and anisotropy  $\kappa = 1.5$ . The dot-dash curve for  $d = -0.4$  takes  $J_{1y}/J_{1x} = 1.5$ .

bounds for the Berry curvature can be found on the upper left and lower right boundaries of the BZ where the magnon modes were degenerate and the Berry curvature vanished for  $J_{1y}/J_{1x} = 1$ .

In Appendix D, we construct a ribbon with edges along the zigzags to demonstrate that nontrivial topological edge modes are associated with the model when the Chern numbers are  $\pm 1$ . No such edge modes appear when the Chern numbers are undefined or 0.

## VI. DISCUSSION AND CONCLUSION

The magnon Hall effect was first predicted for a FM kagomé lattice [18] with DM interactions due to broken inversion symmetry. The subsequent observation and theory of the magnon Hall effect was performed for FM pyrochlore systems [5,6]. Nonzero Berry curvatures and Chern numbers were also suggested for the FM star lattice [33], which has similarities to both kagomé and HC lattices. Earlier work predicted [24,34,35] that OAM can be observed in FM HC lattices. Our current paper predicts that OAM can also be observed in FM ZZ lattices with distinct exchange interactions  $0 < J_1 < J_2$  and  $D \neq 0$ . As shown in Appendixes B and C, OAM is not observable in AF HC and ZZ geometries even when  $D \neq 0$ .

The finite Berry curvatures in both FM HC and ZZ models implies that their transverse thermal conductivities are nonzero. The magnon Hall effect [28] is evaluated in terms of the Berry curvature using Eq. (3), where

$$c_2(\rho) = (1 + \rho) \left( \log \frac{1 + \rho}{\rho} \right)^2 - (\log \rho)^2 - 2\text{Li}_2(-\rho) \quad (55)$$

and  $\text{Li}_2(z)$  is the dilogarithmic function. To account for the different scaling of the magnon energies  $\epsilon_n(\mathbf{k}) = \hbar\omega_n(\mathbf{k})$  for the two FM models, we define  $\tilde{T} = k_B T / 3JS$  and  $\tilde{\kappa}^{xy} = \hbar\kappa^{xy} / 3k_B JS$  (HC) or  $\tilde{T} = k_B T / 2(J_1 + J_2)S$  and  $\tilde{\kappa}^{xy} = \hbar\kappa^{xy} / 2k_B (J_1 + J_2)S$  (ZZ) with the dimensionless thermal

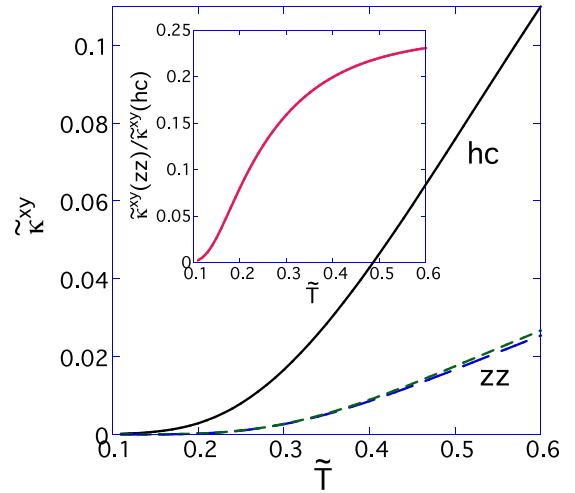


FIG. 13. The normalized thermal conductivity  $\tilde{\kappa}^{xy}(\tilde{T})$  of the FM HC (solid) and ZZ (long dash) models vs  $\tilde{T}$ . Both models take  $d = -0.4$  and  $\kappa = 1.5$ , while the FM ZZ model also uses  $r = 10$  and the upper (small dash) ZZ curve sets  $J_{1y}/J_{1x} = 1.5$ . The inset plots the ratio of the normalized thermal conductivities of the ZZ and HC lattices vs  $\tilde{T}$  with  $J_{1y}/J_{1x} = 1$ .

conductivity given by

$$\tilde{\kappa}^{xy}(\tilde{T}) = -\frac{\tilde{T}}{2\pi} \sum_n \int_{\text{BZ}} d^2k c_2(\rho(\epsilon_n(\mathbf{k}))) \Omega_{nz}(\mathbf{k}) \quad (56)$$

for both models.

To examine the effect of the ratio  $r = J_2/J_1 > 1$  for the FM ZZ model, we plot  $\tilde{\kappa}^{xy}(\tilde{T})$  versus  $r$  for several values of  $d$  in Fig. 12, which sets  $\tilde{T} = 0.3$ , and  $\kappa = 1.5$ . As expected,  $\tilde{\kappa}^{xy}(\tilde{T}) \rightarrow 0$  as  $r \rightarrow 1$ . More unexpectedly,  $\tilde{\kappa}^{xy}(\tilde{T})$  reaches a plateau at about  $r \approx 6$ , which implies that the magnon Hall effect will be most easily observed in materials with large  $r$ .

The magnon Hall effect has been observed in experimental realizations of the pyrochlore [5,6] and kagomé [8] lattices. Unfortunately, it has not yet been observed in FM HC lattices like  $\text{CrBr}_3$  [36] and  $\text{CrIr}_3$  [37]. Nevertheless, we compare theoretical values of  $\tilde{\kappa}^{xy}(\tilde{T})$  for the FM HC and ZZ models in Fig. 13. Taking  $r = 10$  for the FM ZZ model and setting  $\tilde{T} \approx 0.6$ , we find that  $\tilde{\kappa}^{xy}(\tilde{T})$  is about four times larger for the HC model than for the ZZ model. The suppression of the FM state with temperature can always be alleviated by increasing the anisotropy  $K$ .

To estimate the effect of the partially gapped magnons on the ZZ model, we plot the thermal conductivities with  $J_{1y}/J_{1x} = 1.5$  in Figs. 12 and 13. Notice that the magnon band gap produced by  $J_{1y}/J_{1x} = 1.5$  enhances  $\tilde{\kappa}^{xy}(\tilde{T})$  only slightly, with the largest change at small  $r$  in Fig. 12. So the disappearance of the magnon band gap and the absence of a well-defined Chern number when  $J_{1y}/J_{1x} = 1$  does not significantly depress the magnon thermal conductivity at large  $r$ .

Due to the low contrast between different FM exchange couplings, it is difficult to identify materials described by the FM ZZ geometry. Nevertheless, several cases of FM ZZ chains coupled by FM exchange interactions have been discovered: spin-1/2 Heisenberg vanadium chains in  $\text{CdVO}_3$  [38,39], spin-3/2 chromium chains in  $\text{LaCrOS}_2$  [40], and

spin-3.4/2 manganese chains in  $\text{La}_3\text{MnAs}_5$  [41]. For  $\text{CdVO}_3$  [38,39], the intrachain coupling  $J_2 \approx 90$  K is significantly stronger than the interchain coupling  $J_1 \approx 18$  K so that  $r \approx 5$ . For  $\text{La}_3\text{MnAs}_5$  [41],  $r \approx 7.6$ . The exchange ratio  $r$  is also believed to be large in  $\text{LaCrOS}_2$  [40]. As predicted by Fig. 12, observation of the magnon Hall effect depends sensitively on the ratio  $r = J_2/J_1$ . With such large values of  $r$ , any of the materials mentioned above will be good candidates to search for the magnon Hall effect in FM ZZ geometries.

Edge currents produced by the Berry curvature [19,20,29] and closely connected with the thermal conductivity and Chern number [30,31] are only topologically protected in systems containing a gap between the magnon bands, i.e., in magnetic insulators. Therefore, the edge currents in FM ZZ lattices with  $J_{1y}/J_{1x} = 1$  are not topologically protected and will decay with time due to the degenerate  $\mathbf{k}$ -space regions along the  $k_x - k_y = \pm\pi/a$  BZ boundaries where the magnon bands overlap. The topological protection afforded by the symmetry breaking  $J_{1y}/J_{1x} \neq 1$  of the exchange interaction  $J_1$  may then depend on the size of the resulting magnon band gap compared to the temperature and the magnon interactions [42].

Direct observation of the angular-averaged magnon OAM  $F_n(k)$  may be possible in both HC and ZZ lattices by coupling magnons to other particles and quasiparticles. While the dynamics of  $F_n(k)$  remains unexplored, we speculate that the magnon OAM may appear in inelastic neutron scattering experiments through the angular-averaged  $S(\mathbf{k}, \omega)$ , i.e., the powder-averaged  $S(k, \omega)$ , when  $\omega$  crosses a magnon band and  $k$  crosses a peak in  $F_n(k)$ . Alternatively, it may be possible to couple magnons to chiral phonons in either FM honeycomb or zigzag materials. For example, chiral phonons and their quasiparticle couplings have been observed in the honeycomb structure  $\text{WSe}_2$  [25] while the FM zigzag material  $\text{La}_3\text{MnAs}_5$  has a  $6_3$  screw axis that supports phonons with OAM [43]. It may also be possible to couple the magnons to a high-energy electron beam after the electrons are separated into orbital components by a grating [26]. A STEM can then be used to probe the coupling between the electron and magnon OAM when the transverse linear electron momentum matches the linear magnon momentum.

To conclude, we have studied a new class of materials associated with FM ZZ geometries where the effects of OAM are observable. Formally, results for the OAM and Berry curvature for this geometry are quite similar to well-known results for the FM HC lattice. While the magnon bands are not completely gapped, and the Chern numbers are not well defined for  $J_{1y}/J_{1x} = 1$ , those deficits do not significantly impact the magnon transverse thermal conductivity  $\kappa^{xy}(T)$  in ZZ lattices. Indeed, opening a magnon band gap and producing well-defined Chern numbers by setting  $J_{1y}/J_{1x} \neq 1$  only modestly enhances  $\kappa^{xy}(T)$ . Although only an infinitesimal difference  $J_{1y}/J_{1x} - 1 \neq 0$  is required to create a magnon gap, FM ZZ lattice materials with  $J_{1y}/J_{1x} = 1$  are not topological insulators. Consequently, the usefulness of these materials for specific applications may depend on the lifetime of the edge modes. Nonetheless, we are hopeful that future experiments on some of the materials discussed above will demonstrate that the effects of OAM may be observed in systems that are neither topological nor magnetic insulators.

The data that support the findings of this study are available from the authors upon reasonable request.

## ACKNOWLEDGMENTS

Conversations with Shulei Zhang are gratefully acknowledged. Research by R.F., L.L., and T.B. was sponsored by the U.S. Department of Energy, Office of Science, Basic Energy Sciences, Materials Sciences and Engineering Division. Theoretical contributions by J.V. were supported by the U.S. Department of Energy, Office of Science, National Quantum Information Science Research Centers, Quantum Science Center. This manuscript has been authored in part by UT-Battelle, LLC, under Contract No. DE-AC05-00OR22725 with the U.S. Department of Energy (DOE). The U.S. government retains and the publisher, by accepting the article for publication, acknowledges that the U.S. government retains a nonexclusive, paid-up, irrevocable, worldwide license to publish or reproduce the published form of this manuscript, or allow others to do so, for U.S. government purposes. DOE will provide public access to these results of federally sponsored research in accordance with the DOE Public Access Plan [44].

## APPENDIX A: TILING OAM

For the FM ZZ lattice, the smoothness of the even part of the OAM at the zone boundaries is ensured if  $O_{1,2}^{(\text{even})}(k_x, k_y) = O_{1,2}^{(\text{even})}(k_y, k_x)$ , as seen numerically in Figs. 3 and 7. For this case, a point just outside the BZ can be mapped into the corresponding point on the opposite side of the boundary just inside the BZ by using

$$O_{1,2}^{(\text{even})}(\mathbf{k}) = O_{1,2}^{(\text{even})}(\mathbf{k} + \mathbf{G}) \quad (\text{A1})$$

and

$$O_{1,2}^{(\text{even})}(k_x, k_y) = O_{1,2}^{(\text{even})}(-k_y, -k_x), \quad (\text{A2})$$

where  $\mathbf{G}$  is a reciprocal-lattice vector and we have used the even property of  $O_{1,2}^{(\text{even})}(\mathbf{k})$ . Thus, in approaching the BZ edge, the even OAM of point  $\mathbf{k}$  and its mirror across the BZ boundary are equivalent, all the way to the limit of the boundary itself. To show that  $O_{1,2}^{(\text{even})}(k_x, k_y) = O_{1,2}^{(\text{even})}(k_y, k_x)$  for the FM ZZ square lattice, we see that  $O_{1,2}^{(\text{even})}(\mathbf{k})$  in Eq. (48) is composed of functions that are symmetric or antisymmetric with respect to switching components:  $\Psi_{(k_x, k_y)} = \Psi_{(k_y, k_x)}$ ,  $\tau_{(k_x, k_y)} = -\tau_{(k_y, k_x)}$ ,  $\mu_{(k_x, k_y)} = \mu_{(k_y, k_x)}$ , and  $\hat{l}_z(k_x, k_y) = -\hat{l}_z(k_y, k_x)$ . Plugging these into Eq. (48), the negative signs from the antisymmetric terms cancel and  $O_{1,2}^{(\text{even})}(k_x, k_y) = O_{1,2}^{(\text{even})}(k_y, k_x)$ .

## APPENDIX B: AF HONEYCOMB LATTICE

This Appendix considers the HC lattice sketched in Fig. 1(b) with AF exchange  $J < 0$  between alternating up and down spins. We then find

$$\underline{L}(\mathbf{k}) = -\frac{3JS}{2} \begin{pmatrix} A_{\mathbf{k}}^+ & 0 & 0 & -\Gamma_{\mathbf{k}}^* \\ 0 & A_{\mathbf{k}}^+ & -\Gamma_{\mathbf{k}} & 0 \\ 0 & -\Gamma_{\mathbf{k}}^* & A_{\mathbf{k}}^- & 0 \\ -\Gamma_{\mathbf{k}} & 0 & 0 & A_{\mathbf{k}}^- \end{pmatrix}, \quad (\text{B1})$$

where  $A_{\mathbf{k}}^{\pm} = 1 \pm d \Theta_{\mathbf{k}} + \kappa$  as in the FM HC lattice but with  $\kappa = 2K/3|J|$ . It is then easy to show that solutions for the eigenfunctions  $X_{rn}^{-1}(\mathbf{k})$  are independent of  $d$ . The doubly degenerate magnon energies

$$\hbar\omega_{1,2}(\mathbf{k}) = 3|J|S\sqrt{(1 + \kappa)^2 - |\Gamma_{\mathbf{k}}|^2} + d \Theta_{\mathbf{k}} \quad (\text{B2})$$

are simply shifted by the DM interaction. As expected,  $O_n(\mathbf{k})$  is an odd function of  $\mathbf{k}$  for any gauge. Therefore, the AF HC lattice does not support an observable OAM and  $F_n(k) = 0$ . However, the AF HC lattice does support the magnon Nernst effect with a net spin current [45,46].

### APPENDIX C: AF ZIGZAG LATTICE

This Appendix treats the AF ZZ lattice with AF coupling  $J_1 < 0$  between chains and FM coupling  $J_2 > 0$  within chains. As seen in Fig. 1(d), the magnetic unit cell contains four spins so the  $\underline{L}(\mathbf{k})$  matrix is eight-dimensional. Fortunately, we can write

$$\begin{aligned} H_2 &= \sum_{\mathbf{k}} \mathbf{v}_{\mathbf{k}}^{\dagger} \cdot \underline{L}(\mathbf{k}) \cdot \mathbf{v}_{\mathbf{k}} \\ &= \sum_{\mathbf{k}} \{ \mathbf{v}_{1\mathbf{k}}^{\dagger} \cdot \underline{L}_1(\mathbf{k}) \cdot \mathbf{v}_{1\mathbf{k}} + \mathbf{v}_{2\mathbf{k}}^{\dagger} \cdot \underline{L}_2(\mathbf{k}) \cdot \mathbf{v}_{2\mathbf{k}} \}, \end{aligned} \quad (\text{C1})$$

where

$$\mathbf{v}_{1\mathbf{k}} = (a_{\mathbf{k}}^{(1)}, a_{\mathbf{k}}^{(2)}, a_{-\mathbf{k}}^{(3)\dagger}, a_{-\mathbf{k}}^{(4)\dagger}), \quad (\text{C2})$$

$$\mathbf{v}_{2\mathbf{k}} = (a_{\mathbf{k}}^{(3)}, a_{\mathbf{k}}^{(4)}, a_{-\mathbf{k}}^{(1)\dagger}, a_{-\mathbf{k}}^{(2)\dagger}), \quad (\text{C3})$$

$$\underline{L}_1(\mathbf{k}) = S(J_2 - J_1) \begin{pmatrix} A_{\mathbf{k}}^{-} & -\gamma_2 \xi_{\mathbf{k}} & 0 & \gamma_1 \xi_{\mathbf{k}}^* \\ -\gamma_2 \xi_{\mathbf{k}}^* & A_{\mathbf{k}}^{+} & \gamma_1 \xi_{\mathbf{k}} & 0 \\ 0 & \gamma_1 \xi_{\mathbf{k}}^* & A_{\mathbf{k}}^{-} & -\gamma_2 \xi_{\mathbf{k}} \\ \gamma_1 \xi_{\mathbf{k}} & 0 & -\gamma_2 \xi_{\mathbf{k}}^* & A_{\mathbf{k}}^{+} \end{pmatrix}, \quad (\text{C4})$$

$$\underline{L}_2(\mathbf{k}) = S(J_2 - J_1) \begin{pmatrix} A_{\mathbf{k}}^{+} & -\gamma_2 \xi_{\mathbf{k}} & 0 & \gamma_1 \xi_{\mathbf{k}}^* \\ -\gamma_2 \xi_{\mathbf{k}}^* & A_{\mathbf{k}}^{-} & \gamma_1 \xi_{\mathbf{k}} & 0 \\ 0 & \gamma_1 \xi_{\mathbf{k}}^* & A_{\mathbf{k}}^{+} & -\gamma_2 \xi_{\mathbf{k}} \\ \gamma_1 \xi_{\mathbf{k}} & 0 & -\gamma_2 \xi_{\mathbf{k}}^* & A_{\mathbf{k}}^{-} \end{pmatrix}, \quad (\text{C5})$$

with  $A_{\mathbf{k}}^{\pm} = 1 \pm d \tau_{\mathbf{k}}$ ,  $d = 2D/(J_2 - J_1)$ , and  $\gamma_n = J_n/2(J_2 - J_1)$ . The only difference between  $\underline{L}_1(\mathbf{k})$  and  $\underline{L}_2(\mathbf{k})$  is that  $D$  changes sign. It is straightforward to show that the symmetry relations of Eqs. (14) and (15) are satisfied by the full matrix  $\underline{L}(\mathbf{k})$ .

The AF ZZ model then contains four magnon bands, which are doubly degenerate with energies

$$\begin{aligned} \hbar\omega_{1,3}(\mathbf{k}) &= 2(J_2 - J_1)S \{ 1 - (\gamma_1^2 - \gamma_2^2) |\xi_{\mathbf{k}}|^2 + 16(d \tau_{\mathbf{k}})^2 \\ &\quad \pm \sqrt{\gamma_2^2 (\gamma_1^2 (\xi_{\mathbf{k}}^2 - \xi_{\mathbf{k}}^{*2})^2 + 4 |\xi_{\mathbf{k}}|^2) + 4(d \tau_{\mathbf{k}})^2} \}^{1/2}, \end{aligned} \quad (\text{C6})$$

$\omega_2(\mathbf{k}) = \omega_1(\mathbf{k})$ , and  $\omega_4(\mathbf{k}) = \omega_3(\mathbf{k})$ . Since the magnon energy does not depend on the sign of  $d$ , lower bands 1 and 2 and upper bands 3 and 4 from  $\underline{L}_1(\mathbf{k})$  and  $\underline{L}_2(\mathbf{k})$  are degenerate.

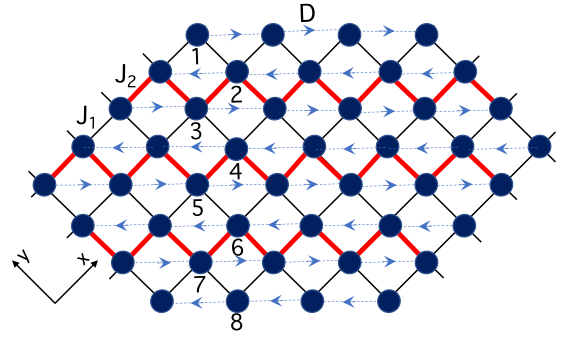


FIG. 14. A ribbon with width  $M = 8$  containing weaker bonds  $J_{1n}$  at the outer edges. The termination is only at the top and bottom; the ribbon propagates to infinity in the other directions.

Additional exchange interactions do not affect the structure of the  $\underline{L}_n(\mathbf{k})$  matrices. For example, an exchange interaction  $J_3$  between spin pairs  $\{1, 3\}$  and  $\{2, 4\}$  along the  $(1,1)$  diagonal does not couple the  $\underline{L}_1(\mathbf{k})$  and  $\underline{L}_2(\mathbf{k})$  matrices. Nor do any other complex set of exchange interactions or anisotropies. So the partition of  $\underline{L}(\mathbf{k})$  into two  $4 \times 4$  matrices remains unaltered.

Numerical calculation of  $F_n(k)$  reveals that  $F_1(k) = -F_2(k)$  and  $F_3(k) = -F_4(k)$  so that the contributions of the two  $\underline{L}_n(\mathbf{k})$  matrices with opposite  $D$  cancel. Hence, there is no net observable OAM from the two lower or two upper magnon bands. Similarly, we find that the Berry curvatures of bands 1 and 2 cancel, as do the Berry curvatures of bands 3 and 4.

### APPENDIX D: EDGE MODES FOR THE ANISOTROPIC FM ZIGZAG LATTICE

The anisotropic FM ZZ model has Chern numbers  $C_n = \pm 1$  when  $\Delta J_1 > \Delta J_2$ ,  $C_n = 0$  when  $\Delta J_2 > \Delta J_1$ , and  $C_n$  undefined when  $\Delta J_1 = \Delta J_2$ , all with the understanding that  $r > 1$ . In this Appendix, we show that a ribbon cut along the zigzags contains topological edge modes only when  $\Delta J_1 > \Delta J_2$ .

There are three ways to construct a ribbon with width  $M$ : with the outer bonds given by the stronger exchange interactions  $J_{2n}$  ( $M$  even), given by the weaker exchange interactions  $J_{1n}$  ( $M$  even), or with  $J_{2n}$  on one side and  $J_{1n}$  on the other ( $M$  odd). In Fig. 14, we have sketched a ribbon with  $M = 8$  and the outer bonds given by  $J_{1n}$ . For this kind of ribbon, the  $2M \times 2M$   $\underline{L}(\mathbf{k})$  matrix is constructed by taking

$$\begin{aligned} L_{11}(\mathbf{k}) &= L_{MM}(\mathbf{k}) = \frac{S}{2}(J_{1x} + J_{1y}) \\ &\quad \mp \frac{SJ_t}{2} d \sin(k_y a - k_x a), \end{aligned} \quad (\text{D1})$$

$$\begin{aligned} L_{rr}(\mathbf{k}) &= \frac{SJ_t}{2} + \frac{SJ_t}{2} (-1)^r d \sin(k_y a - k_x a), \\ r &\neq 1, M, \end{aligned} \quad (\text{D2})$$

$$L_{r,r+1}(\mathbf{k}) = -\frac{S}{2}(J_{nx} e^{-ik_x a} + J_{ny} e^{-ik_y a}), \quad (\text{D3})$$

with  $n = 1$  for  $r$  odd and  $n = 2$  for  $r$  even. We also have  $L_{r+1,r}(\mathbf{k}) = L_{r,r+1}(\mathbf{k})^*$  for  $r$  both odd or even. Note that in all matrix elements  $L_{rs}(\mathbf{k})$ ,  $r$  and  $s$  are assumed to be less

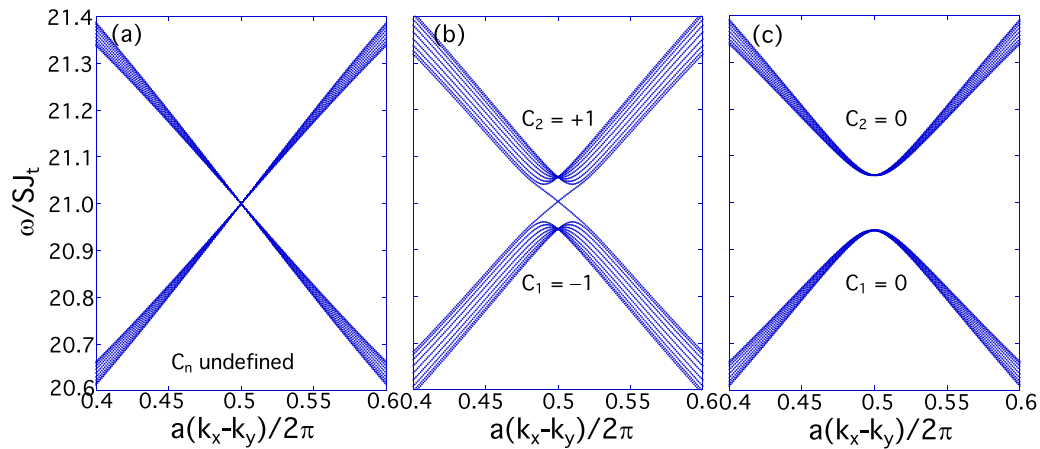


FIG. 15. The frequencies  $\omega/SJ_t$  for a ribbon with width  $M = 20$  containing weaker bonds  $J_{1n}$  at the outer edges and (a)  $J_{1x} = J_{1y} = 1$ ,  $J_{2x} = J_{2y} = 8$ ; (b)  $J_{1x} = 0.5$ ,  $J_{1y} = 1.5$ ,  $J_{2x} = J_{2y} = 8$ ; or (c)  $J_{1x} = J_{1y} = 1$ ,  $J_{2x} = 7$ ,  $J_{2y} = 8$ , all with  $\kappa = 10$  and  $d = -0.4$ .

than or equal to  $M$ . Then the matrix elements  $L_{r+M,s+M}(\mathbf{k})$  are determined by using Eq. (14).

The differences between the outer and inner bonds are that the outer bonds have different diagonal terms  $L_{11}(\mathbf{k})$  and  $L_{MM}(\mathbf{k})$  because they only couple to interior sites through the weaker exchange interactions  $J_{1n}$ . Also sites 1 couple only downwards to sites 2 and sites  $M$  only couple upwards to sites  $M - 1$  through those weaker bonds. Notice that the DM interaction alternates directions from the top of the ribbon to the bottom, but its strength remains the same.

Results for the modes of this type of ribbon are shown in Fig. 15. In Fig. 15(a) with  $\Delta J_1 = \Delta J_2 = 0$ , the Chern

number  $C_n$  is undefined and there is no gap due to the absence of  $xy$  anisotropy. In Fig. 15(b) with  $\Delta J_2 > \Delta J_1 = 0$ , a band gap appears due to the  $xy$  anisotropy in  $J_{1n}$ . Topological edge modes are associated with the Chern numbers  $C_1 = -1$  and  $C_2 = +1$ . In Fig. 15(c) with  $\Delta J_2 > \Delta J_1 = 0$ , a band gap once again appears due to the  $xy$  anisotropy (now in  $J_{2n}$ ) but the edge modes are absent and  $C_1 = C_2 = 0$ . Hence, there is a clear connection between our earlier results for the Chern numbers and the appearance of topological edge modes on a ribbon. This is called [29] the bulk-edge or bulk-boundary correspondence.

- [1] X. S. Wang and X. R. Wang, Topological magnonics, *J. Appl. Phys.* **129**, 151101 (2021).
- [2] A. V. Chumak, P. Kabos, M. Wu, C. Abert, C. Adelman, A. O. Adeyeye, J. Åkerman, F. G. Aliev, A. Anane, A. Awad, C. H. Back, A. Barman, G. E. W. Bauer, M. Becherer, E. N. Beginin, V. A. S. V. Bittencourt, Y. M. Blanter, P. Bortolotti, I. Boventer, D. A. Bozhko, S. A. Bunyaev, J. J. Carmiggelt, R. R. Cheenikundil, F. Ciubotaru, S. Cotozana, G. Csaba, O. V. Dobrovolskiy, C. Dubs, M. Elyasi, K. G. Fripp, H. Fulara, I. A. Golovchanskiy, C. Gonzalez-Ballester, P. Graczyk, D. Grundler, P. Gruszecki, G. Gubbiotti, K. Guslienko, A. Haldar, S. Hamdioui, R. Hertel, B. Hillebrands, T. Hioki, A. Houshang, C.-M. Hu, H. Huebl, M. Huth, E. Iacocca, M. B. Jungfleisch, G. N. Kakazei, A. Khitun, R. Khymyn, T. Kikkawa, M. Kläui, O. Klein, J. W. Kłos, S. Knauer, S. Koraltan, M. Kostylev, M. Krawczyk, I. N. Krivorotov, V. V. Kruglyak, D. Lachance-Quirion, S. Ladak, R. Lebrun, Y. Li, M. Lindner, R. Macêdo, S. Mayr, G. A. Melkov, S. Mieszczak, Y. Nakamura, H. T. Nembach, A. A. Nikitin, S. A. Nikitov, V. Novosad, J. A. Otálora, Y. Otani, A. Papp, B. Pigeau, P. Pirro, W. Porod, F. Porrati, H. Qin, B. Rana, T. Reimann, F. Riente, O. Romero-Isart, A. Ross, A. V. Sadovnikov, A. R. Safin, E. Saitoh, G. Schmidt, H. Schultheiss, K. Schultheiss, A. A. Serga, S. Sharma, J. M. Shaw, D. Suess, O. Surzhenko, K. Szulc, T. Taniguchi, M. Urbánek, K. Usami, A. B. Ustinov,

- T. van der Sar, S. van Dijken, V. I. Vasyuchka, R. Verba, S. Viola Kusminskiy, Q. Wang, M. Weides, M. Weiler, S. Wintz, S. P. Wolski, and X. Zhang, Advances in magnetism roadmap on spin-wave computing, *IEEE Trans. Magn.* **58**, 1 (2022).
- [3] D. D. Sheka, O. V. Pylypovskiy, O. M. Volkov, K. V. Yershov, V. P. Kravchuk, and D. Makarov, Fundamentals of curvilinear ferromagnetism: statics and dynamics of geometrically curved wires and narrow ribbons, *Small* **18**, 2105219 (2022).
- [4] O. Büttner, M. Bauer, A. Rueff, S. O. Demokritov, B. Hillebrands, A. N. Slavin, M. P. Kostylev, and B. A. Kalinikos, Space- and time-resolved Brillouin light scattering from nonlinear spin-wave packets, *Ultrasonics* **38**, 443 (2000).
- [5] Y. Onose, T. Ideue, H. Katsura, Y. Shiomi, N. Nagaosa, and Y. Tokura, Observation of the magnon Hall effect, *Science* **329**, 297 (2010).
- [6] T. Ideue, Y. Onose, H. Katsura, Y. Shiomi, S. Ishiwata, N. Nagaosa, and Y. Tokura, Effect of lattice geometry on magnon Hall effect in ferromagnetic insulators, *Phys. Rev. B* **85**, 134411 (2012).
- [7] M. Hirschberger, J. W. Krizan, R. J. Cava, and N. P. Ong, Large thermal Hall conductivity of neutral spin excitations in a frustrated quantum magnet, *Science* **348**, 106 (2015).
- [8] M. Hirschberger, R. Chisnell, Y. S. Lee, and N. P. Ong, Thermal Hall effect of spin excitations in a kagome magnet, *Phys. Rev. Lett.* **115**, 106603 (2015).

- [9] S. Murakami and A. Okamoto, Thermal Hall effect of magnons, *J. Phys. Soc. Jpn.* **86**, 011010 (2017).
- [10] R. R. Neumann, A. Mook, J. Henk, and I. Mertig, Thermal Hall effect of magnons in collinear antiferromagnetic insulators: signatures of magnetic and topological phase transitions, *Phys. Rev. Lett.* **128**, 117201 (2022).
- [11] K.-I. Uchida, H. Adachi, T. Ota, H. Nakayama, S. Maekawa, and E. Saitoh, Observation of longitudinal spin-Seebeck effect in magnetic insulators, *Appl. Phys. Lett.* **97**, 172505 (2010).
- [12] S. M. Wu, W. Zhang, A. KC, P. Borisov, J. E. Pearson, J. S. Jiang, D. Lederman, A. Hoffmann, and A. Bhattacharya, Antiferromagnetic spin Seebeck effect, *Phys. Rev. Lett.* **116**, 097204 (2016).
- [13] A. Okamoto and S. Murakami, Berry curvature for magnons in ferromagnetic films with dipole-exchange interactions, *Phys. Rev. B* **96**, 174437 (2017).
- [14] J. Liu, L. Wang, and K. Shen, Spin-orbit coupling and linear crossings of dipolar magnons in van der Waals antiferromagnets, *Phys. Rev. B* **102**, 144416 (2020).
- [15] M. C. Chang and Q. Niu, Berry Phase, Hyperorbits, and the Hofstadter spectrum: semiclassical dynamics in magnetic Bloch bands, *Phys. Rev. B* **53**, 7010 (1996).
- [16] G. Sundaram and Q. Niu, Wave-packet dynamics in slowly perturbed crystals: gradient corrections and Berry-phase effects, *Phys. Rev. B* **59**, 14915 (1999).
- [17] D. Xiao, M. C. Chang, and Q. Niu, Berry phase effects on electronic properties, *Rev. Mod. Phys.* **82**, 1959 (2010).
- [18] H. Katsura, N. Nagaosa, and P. A. Lee, Theory of the thermal Hall effect in quantum magnets, *Phys. Rev. Lett.* **104**, 066403 (2010).
- [19] R. Matsumoto and S. Murakami, Theoretical prediction of a rotating magnon wave packet in ferromagnets, *Phys. Rev. Lett.* **106**, 197202 (2011).
- [20] R. Matsumoto and S. Murakami, Rotational motion of magnons and the thermal Hall effect, *Phys. Rev. B* **84**, 184406 (2011).
- [21] V. M. Tsukernik, Some features of the gyromagnetic effect in ferro dielectrics at low temperatures, *Sov. J. Exp. Theor. Phys.* **50**, 1631 (1966).
- [22] V. S. Garmatyuk and V. M. Tsukernik, The gyromagnetic effect in an antiferromagnet at low temperatures, *Sov. J. Exp. Theor. Phys.* **26**, 1035 (1968).
- [23] T. Fukui, Y. Hatsugai, and H. Suzuki, Chern numbers in discretized Brillouin zone: efficient method of computing (spin) Hall conductances, *J. Phys. Soc. Jpn.* **74**, 1674 (2005).
- [24] R. S. Fishman, Gauge-invariant measure of the magnon orbital angular momentum, *Phys. Rev. B* **107**, 214434 (2023).
- [25] H. Zhu, J. Yi, M.-Y. Li, J. Xiao, L. Zhang, C.-W. Yang, R. A. Kaindl, L.-J. Li, Y. Wang, and X. Zhang, Observation of chiral phonons, *Science* **359**, 579 (2018).
- [26] B. J. McMorran, A. Agrawal, P. A. Ercius, V. Grillo, A. A. Herzing, T. R. Harvey, M. Linck, and J. S. Pierce, Origins and demonstrations of electrons with orbital angular momentum, *Philos. Trans. R. Soc. A* **375**, 20150434 (2017).
- [27] R. S. Fishman, J. S. Gardner, and S. Okamoto, Orbital angular momentum of magnons in collinear magnets, *Phys. Rev. Lett.* **129**, 167202 (2022).
- [28] R. Shindou, R. Matsumoto, S. Murakami, and J.-I. Ohe, Topological chiral magnonic edge mode in a magnonic crystal, *Phys. Rev. B* **87**, 174427 (2013).
- [29] R. S. K. Mong and V. Shivamoggi, Edge states and the bulk-boundary correspondence in Dirac Hamiltonians, *Phys. Rev. B* **83**, 125109 (2011).
- [30] L. Zhang, J. Ren, J.-S. Wang, and B. Li, Topological magnon insulator in insulating ferromagnet, *Phys. Rev. B* **87**, 144101 (2013).
- [31] A. Mook, J. Henk, and I. Mertig, Magnon Hall effect and topology in kagome lattices: a theoretical investigation, *Phys. Rev. B* **89**, 134409 (2014).
- [32] W. P. Su, J. R. Schrieffer, and A. J. Heeger, Solitons in polyacetylene, *Phys. Rev. Lett.* **42**, 1698 (1979).
- [33] S. A. Owerre, Topological magnon bands in ferromagnetic star lattice, *J. Phys.: Condens. Matter* **29**, 185801 (2017).
- [34] R. Cheng, S. Okamoto, and D. Xiao, Spin Nernst effect of magnons in collinear antiferromagnets, *Phys. Rev. Lett.* **117**, 217202 (2016).
- [35] S. A. Owerre, Topological honeycomb magnon Hall effect: a calculation of thermal Hall conductivity of magnetic spin excitations, *J. Appl. Phys.* **120**, 043903 (2016).
- [36] Z. Cai, S. Bao, Z.-L. Gu, Y.-P. Gao, Z. Ma, Y. Shangguan, W. Si, Z.-Y. Dong, W. Wang, Y. Wu, D. Lin, J. Wang, K. Ran, S. Li, D. Adroja, X. Xi, S.-L. Yu, X. Wu, J.-X. Li, and J. Wen, Topological magnon insulator spin excitations in the two-dimensional ferromagnet CrBr<sub>3</sub>, *Phys. Rev. B* **104**, L020402 (2021).
- [37] L. Chen, J.-H. Chung, B. Gao, T. Chen, M. B. Stone, A. I. Kolesnikov, Q. Huang, and P. Dai, Topological spin excitations in honeycomb ferromagnet CrI<sub>3</sub>, *Phys. Rev. X* **8**, 041028 (2018).
- [38] M. Onoda and N. Nishiguchi, S=1/2 zigzag-chain structure and ferromagnetism of CdVO<sub>3</sub>, *J. Phys.: Condens. Matter* **11**, 749 (1999).
- [39] A. A. Tsirlin, O. Janson, and H. Rosner, Unusual ferromagnetic superexchange in CdVO<sub>3</sub>: the role of Cd, *Phys. Rev. B* **84**, 144429 (2011).
- [40] Y. Takano, T. Tsubaki, C. Itoi, K. Takase, and K. Sekizawa, Magnetization and specific heat of a ferromagnetic zigzag spin chain compound LaCrO<sub>2</sub>, *Solid State Commun.* **122**, 661 (2002).
- [41] L. Duan, X. C. Wang, J. Zhang, Z. Hu, J. F. Zhao, Y. G. Feng, H. L. Zhang, H.-J. Lin, C. T. Chen, W. Wu, Z. Li, R. Wang, J. F. Zhang, T. Xiang, and C. Q. Jin, Synthesis, structure, and magnetism in the ferromagnet La<sub>3</sub>MnAs<sub>5</sub>: well-separated spin chains coupled via itinerant electrons, *Phys. Rev. B* **106**, 184405 (2022).
- [42] A. Mook, K. Plekhanov, J. Klinovaja, and D. Loss, Interaction-stabilized topological magnon insulator in ferromagnets, *Phys. Rev. X* **11**, 021061 (2021).
- [43] R. Juneja, X. Li, S. Th ebaud, D. H. Moseley, Y. Q. Cheng, M. E. Manley, R. P. Hermann, and L. Lindsay, Phonons in complex twisted crystals: angular momenta, interactions, and topology, *Phys. Rev. B* **106**, 094310 (2022).
- [44] <http://energy.gov/downloads/doe-public-access-plan>.
- [45] S. K. Kim, H. Ochoa, R. Zarzuela, and Y. Tserkovnyak, Realization of the Haldane-Kane-Mele model in a system of localized spins, *Phys. Rev. Lett.* **117**, 227201 (2016).
- [46] Y. Shiomi, R. Takashima, and E. Saitoh, Experimental evidence consistent with a magnon Nernst effect in the antiferromagnetic insulator MnPS<sub>3</sub>, *Phys. Rev. B* **96**, 134425 (2017).